CHARACTERIZATION OF MULTIFUNCTIONAL BIODEGRADABLE – BIOCOMPATIBLE ICG-LOADED NANOPARTICLES AND THEIR FEASIBILITY FOR PROSTATE CANCER IMAGING AND PHOTOTHERAPY

by

RONAK PATEL

Presented to the Faculty of the Graduate School of

The University of Texas at Arlington in Partial Fulfillment

of the Requirements

for the Degree of

MASTER OF SCIENCE IN BIOMEDICAL ENGINEERING

THE UNIVERSITY OF TEXAS AT ARLINGTON

December 2011

ACKNOWLEDGEMENTS

At this juncture, I would like to thank all the people for helping me throughout my work and make this thesis possible.

It is difficult to express my gratitude to my supervisor, Dr. Hanli Liu, who gave me the opportunity to work in her laboratory. She gave inspiration throughout my work and guided and supported me in all the possible ways to improve my skills. During the course of the research, she provided me encouragement, sound advice, good teaching and many ideas to make my thesis better.

I also owe sincere gratitude to Dr. Kytai Nguyen for her advice. I would also like to thank Dr. Nguyen's Laboratory members and, specially, Mr. Aniket Wadajkar for his support in every aspect of my research work. I am sincerely grateful to Dr. Jer-Tsong Hsieh who greatly supported and guided me with the in vivo studies. I am thankful to Dr. Baohong Yuan for accepting my request to be in my committee.

I want to thank my laboratory members, Vikrant and Zi-Jing, for being helpful during my research and also my friends, Yamini and Revathy, for their support. I wish to thank my parents, Mr. and Mrs. Hemant and Jayshree Patel, who raised, supported, taught, loved and inspired me to earn things through hard work and sincerity. Last and most importantly, I would like to thank my husband, Mr. Nimit Patel, for being a source of motivation and his constant support throughout my thesis. To him I dedicate my thesis.

November 15, 2011

ABSTRACT

CHARACTERIZATION OF MULTIFUNCTIONAL BIODEGRADABLE – BIOCOMPATIBLE ICG-LOADED NANOPARTICLES AND THEIR FEASIBILITY FOR PROSTATE CANCER IMAGING AND PHOTOTHERAPY

Ronak Patel, M.S.

The University of Texas at Arlington

Supervised Professor: Dr. Hanli Liu

Prostate cancer is the most common male cancer in the United States, and the second leading cause of cancer death in men. The conventional diagnostic procedures use an invasive approach to collect the biopsy tissue samples. Also, treatments currently used include radiotherapy, chemotherapy and surgical removal of the prostate associated with high risks of surgical complications. Among all the imaging modalities, Near Infrared (NIR) optical imaging could be a possible candidate for minimally invasive diagnosis of prostate cancer with avoidance of harmful radiation and relatively low cost. This motivation brings the development of multifunctional polymeric (di-

lactide-co-glycolic acid) (PLGA) Nanoparticles encapsulating indocyanine green (ICG) which acts as exogenous NIR contrast and thermal agent specific to prostate cancer.

The objective of this study was to evaluate and characterize multi-functionality of biodegradable – biocompatible ICG loaded PLGA nanoparticles as thermal ablation agent for cancer therapy and as an optical contrast agent for prostate cancer imaging. The important parameters for particle characterization such as particle size, polydispersity index and ICG loading efficiency were investigated. For optical characterization of nanoparticles, the excitation – emission matrix, absorption spectra and fluorescence lifetime were determined. The photostability study on the optical parameters reveals the stability of PLGA – ICG Nanoparticles (PIN) in aqueous medium. The human dermal fibroblast (HDF) cell viability study demonstrated the cytotoxicity of PIN. Successful cellular uptake of R11 peptide conjugated PIN with prostate cancer (PC3) cells was obtained. Absorption capability of PIN was also explored as a thermal ablation agent through a phantom study and *ex vivo* tissue phantom studies. Moreover, results of thermal ablation through the phantom study showed an increase of ~ 10 – 12 ˚C in temperature, which is sufficient to create local hyperthermia to treat cancer. The application of PIN as an exogenous contrast was investigated through an *ex vivo* tissue and *in vivo* animal model to examine PIN's ability for enhancing imaging contrast for prostate tumor detection by multi spectral imaging. The results showed great promises, suggesting possible application of PIN towards diagnostic imaging and therapy.

TABLE OF CONTENTS

LIST OF ILLUSTRATIONS

LIST OF TABLES

CHAPTER 1

INTRODUCTION

1.1 Anatomy of Prostate Gland

Prostate gland is an exocrine gland, present in the human male reproductive system, secreting their secretions in ducts, which are directly released in the surrounding environment. Prostate gland is a small walnut shaped organ about 3 cm long located underneath the urinary bladder, above the penis and in front of the rectum as shown in Figure 1.1 below (1,2).

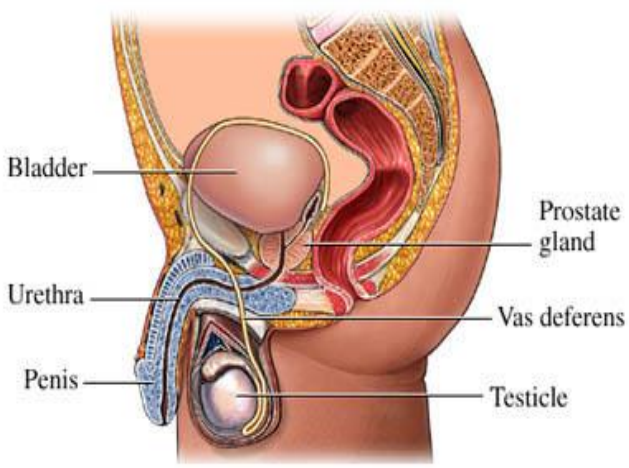

Figure 1.1: Male Reproductive System

The prostate gland is made of glandular and muscular tissue, with ducts opening into the prostatic portion of the urethra. The urethra passes through the center of the prostate, from the bladder to the penis allowing the urine to flow out of the body.

Urethra in males serves a dual purpose. It carries urine from the bladder and also carries semen during the period of ejaculation, through penis. Semen is the sperm carrying, sexual fluid in humans. The prostate gland is encased in pelvic muscles, which contract and aid the ejaculatory process (2,3).

The prostate is divided on the basis of zones and lobes. The zone classification has been specifically meant for medical purposes, where the glandular function of each part is considered to treat any complications. The prostate anatomy can be divided into three zones: peripheral, central, and transitional zone; categorized by the function of the prostate tissue. The peripheral zone is the outermost area of the prostate, resting closest to the wall of the rectum. It makes up approximately 70% of a healthy prostate gland. The next is the central zone, which is approximately 25% of the prostate tissue. This area contains the ejaculatory ducts, which help move semen through the urethra and out of the body. The transitional zone of the prostate, resting next to the urethra, makes up around 5% of the prostate at puberty. This zone continues to increase in size throughout adulthood. The prostate gland anatomy is majorly classified on the basis of lobes and is divided into three lobes: the central lobe and lobes on either side, called the anterior lobes. The central lobe of the prostate is pyramid shaped and rests between the ejaculatory ducts and the urethra. The anterior lobes of the prostate rest near the urethra.

The chief function of prostate gland is the secretion of an alkaline fluid containing citric acid, enzymes and calcium that forms a part of the seminal fluid ejaculated during the male orgasm. The alkalinity of the fluid plays a crucial role in

increasing the life span of the sperms. This fluid makes the semen alkaline, which protects the sperms from hostile acidic environment, on vaginal entry during intercourse. Hence, it aids sperm mobility and survival, ultimately increasing the chances of fertility. During the male orgasm, the muscular glands present in the prostate help the alkaline fluid besides the sperm (produced in the testicles) to propel out through penis. It also controls the flow of urine during ejaculation (1,3).

Hence, the anatomy and functions of the prostate gland reveal its importance and also conceal that any prostate disorder would affect urination, ejaculation and defecation in men which would lead to acute problems.

1.2 Prostate Cancer

Prostate cancer is third leading cause of death from cancer for men of all ages and most commonly for men over age 55 (4). So far the main cause of prostate cancer is unknown, although the risk factors for prostate cancer include advancing age, genetics (heredity), hormonal influences, and such environmental factors as toxins, chemicals, and industrial products. On the other hand, the chances of developing prostate cancer increase with age. Hence, it is rarely found under the age of 40 and most commonly found at the age of about 55-75 years (5,4).

Normally, the prostate starts to develop before birth and further keeps on growing until a man reaches adulthood. The male hormones are responsible for this

continuous growth of prostate. Hence, the prostate gland will not grow to its full size if the levels of male hormones are low (6). In older men, some portion of the prostate around the urethra may keep on growing which leads to a noncancerous condition called Benign Prostatic Hyperplasia (BPH) which further results in problems of passing urine as the prostate can press on the urethra (7). Though BPH is a serious condition but it is not prostate cancer.

Prostate cancer is a malignant tumor that is related to cells from the prostate gland. Mostly it occurs as the cells of prostate mutate and begin to divide out of control. Generally, the tumor growth is slow and it remains confined to the gland for many years. Throughout the time, the tumor shows little or no symptoms or any outward signs. However, for the aggressive types of prostate cancer, the cells grow and spread more rapidly than others and can cause significant symptoms that root to shortening of life. Moreover, with the advancement of cancer, it has the risk of spreading beyond the prostate into the surrounding tissues. Furthermore, the cancer can still spread further and throughout other areas of the body, such as the bones, lungs and liver (5,6). Hence, for men, prostate cancer can become more critical if it is not treated on time and that can lead to death.

1.3 Current Diagnosis methods and Therapy for Prostate Cancer

Prostate cancer is most often discovered by physical examination or screening blood tests which are the standard methods for early cancer detection (7). Physical examination such as Direct Rectal Examination (DRE) is done by the examiner by inserting gloved, lubricated finger into the rectum to examine the size, shape, and texture of the prostate. Screening blood tests, such as the Prostate Specific Antigen (PSA) test measures the blood level of prostate-specific antigen, an enzyme produced by the prostate. Findings of these tests are validated by transrectal ultrasound (TRUS) guided needle biopsy (8) and further confirmed by CT or MRI scans (8). However, the conventional diagnostic methods have certain drawbacks. Techniques such as DRE and PSA fail to differentiate between cancerous and non-cancerous tissue (7). Whereas, TRUS guided biopsy is a "blind" procedure involving quasi-random sampling of the prostate tissue. The implications of this drawback are false negatives, and oversampling of tissue due to non-specific targeting. Moreover, the standard imaging techniques such as MRI, CT or Ultrasonography are not able to detect cancer at early stages and hence, provide limited information regarding disease staging (8). It is therefore imperative to develop a more targeted technique, which can identify the tumor on-site with high sensitivity and specificity as well as at early stage.

Prostate cancer once diagnosed has several treatment options, depending on speed of tumor growth, spreading of tumor, age of the person, and also benefits and drawbacks to treatment. In the early stages when tumor is growing slowly watchful

waiting is recommended which refers regular monitoring without any invasive means. If symptom starts developing medications like chemotherapy or hormone therapy can be used to stop the growth of cancer cells in prostate. Radiation therapy, also known as radiotherapy, uses ionizing radiation to kill prostate cancer cells. It may be used instead of surgery for early cancers, and it may also be used in advanced stages of prostate cancer to treat painful bone metastases. Brachytherapy is a kind of radiotherapy which implants tiny radioactive seeds in the prostate to deliver radiation over a longer time period to kill cancer cells. If radiation therapy fails to stop tumor growth, surgically removal of prostate is the only option to control the cancer growth. Current treatments are associated with high risks of surgical complications. The drawback of these treatments includes toxic effects of the drug, high radiation exposure, and also damage to the non-cancerous parts of the body (4,5,6).

1.4 Motivation of Research

The conventional diagnostic techniques available have shown certain limitations as discussed previously. In recent times, NIR optical imaging showed promising results in imaging prostate through techniques like fluorescence Diffuse Optical Tomography (DOT), and Photoacoustic (PA) imaging (14, 15, 38). Sensitivity of these techniques in visible spectral range is limited. However, imaging in NIR spectral range overcomes this limitation as the blood and biological tissues are comparatively transparent at this wavelength range (650-900 nm) which is shown in Figure 1.2 (11). These techniques

have other advantages such as minimal intrinsic background interference by tissue due to higher penetration depth of light into the biological tissue, avoidance of harmful radiation and relatively low instrumentation/experimental costs (12). Due to these benefits optical imaging techniques are extensively used to monitor tumor perfusion, angiogenesis, oxygenation and tumor growth (12). The ability to detect cancer using optical imaging at the early stage has initiated interest in the development of exogenous optical contrast agents which are specific to cancer as well as have therapeutic abilities. These dual purpose exogenous contrasts can not only provide high sensitivity and acceptable signal-to-noise to optical imaging modalities but also can cure cancer by creating local heating when irradiated by NIR light(12).

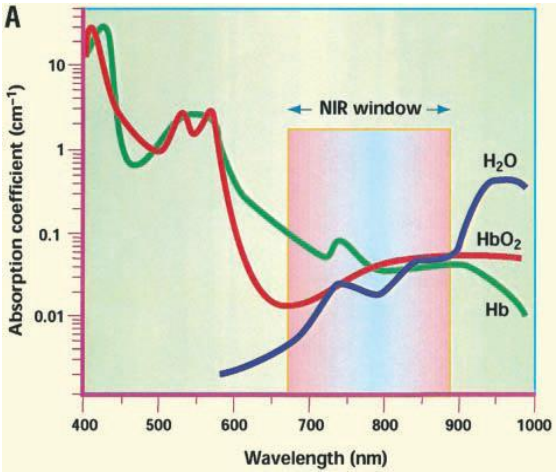

Figure 1.2: Representation of the optical imaging window

The advantage of this technique includes the use of a focused light beam for activation prompting selective killing of tumor cells, low cost, repeatable, minimal side effects and less painful than conventional methods (13,14). Hence, there is an urge to develop multi-functional, biocompatible exogenous contrast agents who can be used as

optical imaging and therapeutic agents. This motivation leads to fabricate biocompatible, biodegradable and multifunctional PLGA ICG Nanoparticles (PIN).

This study covers fabrication of PIN, their optical and structural characterization and also tests their therapeutic and imaging abilities. Success of this project will be a small step towards reducing present complications arising with prostate cancer diagnosing/treatment methods and optimize the quality of life for the patients.

CHAPTER 2

SYNTHESIS AND CHARACTERIZATION OF PIN

2.1 Background

2.1.1 Purpose of PLGA ICG Nanoparticles

Nanotechnology is converting into a revolution in health care for enhanced diagnostic and therapeutic applications for various diseases. Recently, nanoparticle systems have received much consideration towards targeting tumor in a passive manner. On the other hand, nanoparticle encapsulated contrast agents have become conventional for imaging systems (16,17). Several targeting agents have been used in the form of polymeric nanoparticles (18), dendrimers, micelles (19), metallic nanoparticles (20) as well as silica nanoparticles (21). In spite of these large varieties of formulations the use of polymeric nanoparticles has served more attention due to their multifunctional ability. Apart from targeting, when such polymeric nanoparticles are encapsulated with organic dyes like Indocyanine green (18,20), Alexa – fluora (22), IR 800 (23) and texas RED (24); they have shown excellent labeling properties. From the above mentioned nanoparticles formulation and organic dyes: PLGA and ICG have shown more interest as they are biocompatible, biodegradable and approved by Federal Drug Administration (FDA) for clinical use (25,26,27). Therefore, I have chosen PLGA polymer and ICG dye to form the nanoparticulate carrier system.

2.1.2 ICG

Indocyaninc green is an amphiphilic, tricarbocyanine near infrared dye. ICG being a fluorescence dye so when irradiated, strongly absorbs light at 780 nm and fluoresces at 820 nm. (20,29). Also, when irradiated with high energy it absorbs light and converts into heat as seen in Figure 2.1(b). It shows minimal toxic effects hence it is widely used for diagnostic applications such as ophthalmic angiography, cardiac output measurements and diagnostic imaging (24,25).

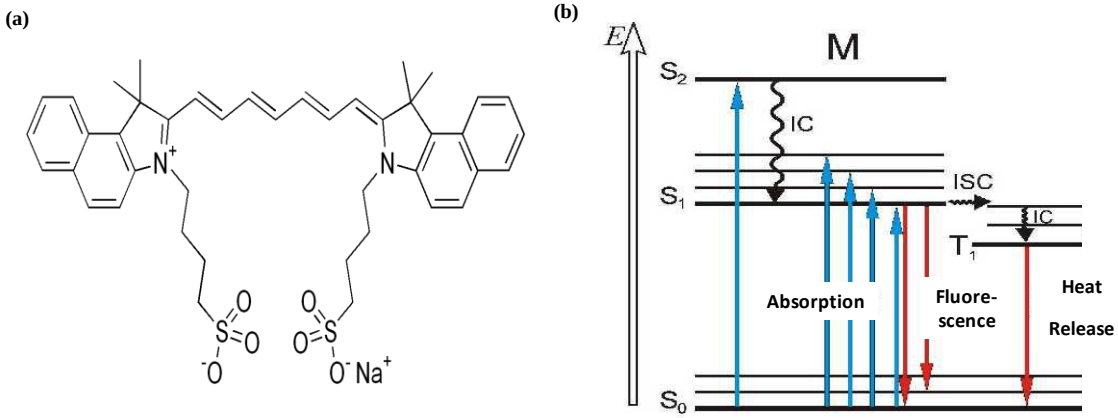

Figure 2.1: (a) Chemical Structure of ICG (b) Energy Diagram for ICG

Recently, much focus is paid on the fluorescence property of ICG that serves as a contrast agent for tumor imaging. Moreover, the strong absorption with NIR light makes it suitable for DOT and PA imaging (15,38). Apart from optical properties, it has shown excellent thermal properties (29). ICG when irradiated by light; absorbs light and converts it into heat which can be used for photothermal treatments. Hence, photodynamic therapy using ICG serves a promising method for the destruction of tumor (29, 30, 31).

Although, ICG shows suitable optical and thermal properties, its use is limited for tumor targeting due to its physiochemical properties. ICG has poor aqueous, thermal and photo stability (27). In aqueous solution such as water, blood, plasma and salt solutions ICG shows rapid aggregation and irreversible reduction in photostability (20, 18). Also, ICG in aqueous solution shows photo or thermal instability when exposed to light or higher temperature (25, 27). ICG when injected in the body shows high protein binding and rapid elimination from the body with a half life of 2 – 4 minutes (25, 27). This leads to low intracellular uptake and minimum binding to tumor sites. Thus the lack of target specificity of ICG limits its application for tumor imaging and therapy (25-31)

2.1.3 PLGA

Poly (Lactic - Co – Glycolic Acid) (PLGA) is a copolymer from the ester family which is formed of two different monomers units lactic acid and glycolic acid as shown in Figure 2.2 . During polymerization, the two monomers are linked to each other by ester linkages. PLGA is amorphous in nature and can be dissolved in a wide range of common solvents. When dissolved in water it hydrolyses, the ester linkages starts breaking and it degrades. Generally the degradation time is dependent on the ratio of the two monomers. Higher the amount of glycolic acid less is the degradation time. The minimum degradation time for PLGA at 50:50 monomer ratio is about 2-4 weeks (33, 34, 36).

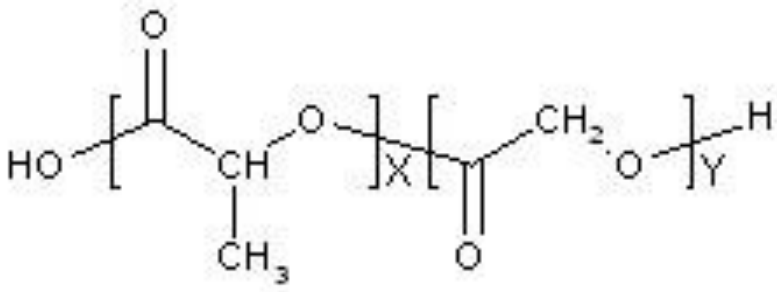

Figure 2.2: Chemical Structure of PLGA where X and Y are number of lactic acid and glycolic acid units (28)

Hence, PLGA has been a successful biodegradable polymer as in the body in presence of water it hydrolysis and gives the two monomer units that are the byproduct of many biological processes taking place in the body. Thus, the two monomers do not produce any toxic adverse effects in the body. Therefore, it is commonly used for various biomedical applications such as grafts, sutures, implants, prosthetic devices and nanoparticles (33,34).

PLGA nanoparticles have been widely used as delivery vehicles for targeting tumor as they show both entrapment of the organic dye and conjugation of the ligand through available functional group. PLGA nanoparticle is associated with Enhanced Permeation and Retention (EPR) effect that allows passive targeting from the blood stream into the tumor site (27,32,35).

Therefore, I employed multifunctional nanoparticulate system entrapping ICG within the PLGA matrix that shows targeting ability for tumor imaging and therapy. The PLGA nanoparticulate system encapsulating ICG retains all the optical and thermal

properties of ICG. Also, PLGA maintains the aqueous, thermal and photo stability of ICG. Moreover, PIN shows a circulation half - life of 14 minutes which is 3-7 times more than the free circulating ICG (27). Thus, when conjugated with a prostate specific peptide; it permits PIN to target prostate tumor for in-vivo tumor imaging as well as for hyperthermia treatments.

2.2 Materials and Methods

2.2.1 Materials

I used ICG, PLGA (DLG -4A 50:50, Lakeshore Biomaterials, Pelham, AL), Polyvinyl alcohol 87 – 89% anhydrous (PVA) and Dichloromethane 99.8% anhydrous (DCM). All the materials were of reagent grade and purchased from Sigma chemical Co (St. Louis, MO) unless specified.

2.2.2 Synthesis of PIN

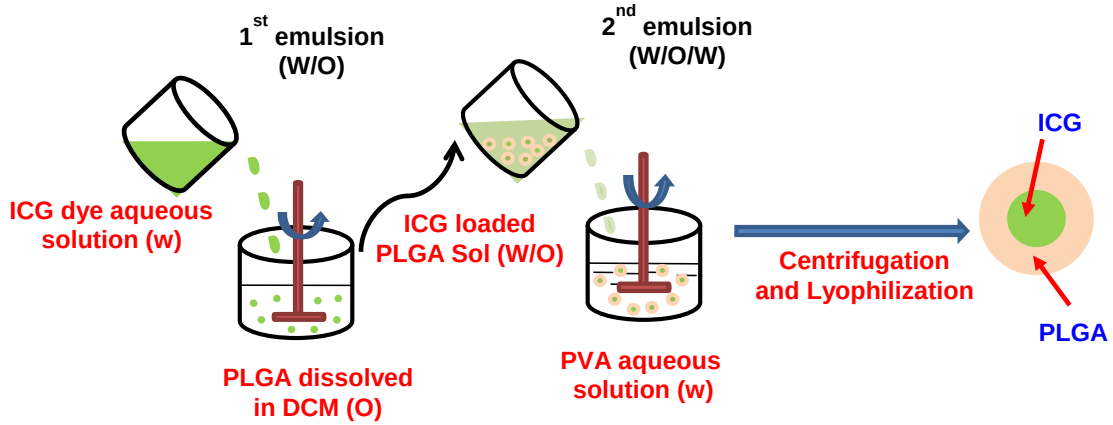

Figure 2.3: Synthesis of PIN by Double Emulsion Process

PIN were formulated by nanoprecipitation method (Double Emulsion Process) (25,33) as shown in Figure 2.3 above. In the beginning 3 solutions were prepared: (1) 5% w/v polyvinyl alcohol (87–89% hydrolyzed) in 12 ml of deionized (DI) water, (2) 90 mg PLGA in 3 ml dichloromethane (99.8%, anhydrous) and (3) 0.25 mM ICG in 1 ml DI water. The first emulsion comprised of drop wise addition of ICG aqueous solution into PLGA organic phase solution; while continuous stirring the PLGA solution at room temperature. The first emulsion thus formed was like mixing water in oil. This will engulf the ICG in PLGA forming droplets of oil loaded with ICG. The first emulsion was further homogenized using an ultrasonic homogenizer (BioLogics Inc., Manassas, VA) at 30 W for 3 minutes to break the droplets into smaller size. The first emulsion was then added dropwise to prepared PVA solution under continuous stirring to form the second emulsion. PVA acts as an emulsifier that maintains uniform particle size and also allows the particles to easily disperse in aqueous medium (34). The second emulsion is like mixing water in oil in water. The solution was then allowed to stir for 1 hour at room temperature at a speed of 1200 rpm using a magnetic stirrer to make sure that DCM gets evaporated. Further, the formed nanoparticles were washed using an ultracentrifuge (Optima XL 90, Beckman, CA) at a high speed of 25000 rpm for 20 minutes at 25 ºC. The supernatant containing non capsulated ICG was then removed and stored at -20 ºC whereas, the palette containing nanoparticles was mixed with DI water. The nanoparticle suspension was then centrifuged (CR3i Multifunctional, Thermo scientific, MO) at 4000 rpm at 25 ºC for 5 minutes in order to separate the aggregates from the nanoparticle suspension. The nanoparticles after

centrifuge were freezed at -20 ºC and later were lyophilized using a FreeZoneBenchtop Freeze Dry Systems (Labconco corporation, Kansas city, MO) to form a powder form of ICG loaded PLGA nanoparticles. The formed PIN were covered with aluminum foil and stored at -20 °C for further use.

2.3 Characterization of PIN

2.3.1 Determination of particle size and surface charge

PINs were characterized in terms of their particle size, polydispersity index and surface charge. 500 µl of nanoparticle solution before the particles are freeze dried was diluted in 1 ml DI water. The solution was homogenized for 3 minutes at 30 W and further measurements were taken. Five different batches of PIN were analyzed on the principle of dynamic light scattering technique using a Zeta Potential Analyzer (ZetaPALS, Brookhaven Inc., NY) and the results are illustrated in Table 1.

Table 2.1: The mean particle size, polydispersity index and surface charge of PIN

	Particle Size (nm)	Polydispersity Index	Surface Charge (mV)
PIN	246.48 ± 10.70	0.10 ± 0.03	-18

The mean particle size of PIN was 246.48 ± 10.70 nm with a polydispersity index of 0.10 ± 0.03 that showed that there was minimal variation in particle size. The surface charge of PIN was found to be -18 mV which infers the stability of PIN.

I studied the structural morphology of the nanoparticle using Scanning Electron Microscope (SEM). PIN formed after freeze dry were diluted thoroughly in DI water to make a final concentration of 1mg/ml. 10µl of nanoparticle solution was added on a glass cover slip and further allowed to dry. The cover slip was coated with silver and then the sample was analyzed using the SEM.

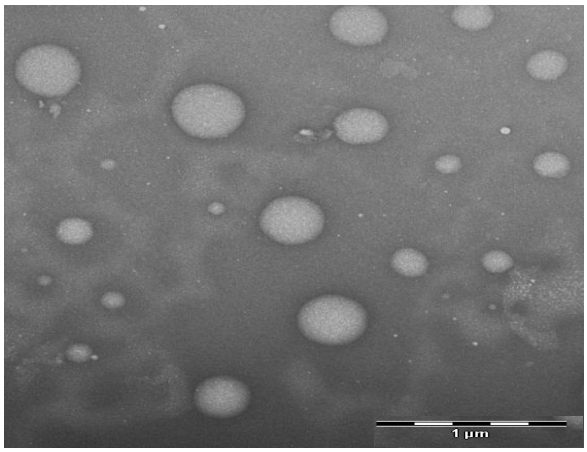

Figure 2.4: SEM image of PIN

The SEM image of PIN as shown in figure 2.4 confirms the spherical shape of PIN and the uniform particle size which was in 250 – 300 nm range.

2.3.2 Determination of ICG loading efficiency in PIN

The ICG loading efficiency was evaluated to determine the amount of ICG free dye encapsulated in PIN. ICG dilutions were prepared by dispersing 50 µg ICG in 1 ml of DI water. Dilutions were formed in between 0.5 – 10 µg/ml of ICG solution. Moreover, 1 ml of supernatant was dissolved in 10 ml of water to measure the ICG content in it. A microplate reader (Infinite M200, TECAN group Ltd., Switzerland) was

used to measure the fluorescence intensity of the ICG solutions and supernatant. Fluorescent intensity of the solutions was measured at an excitation of 780 nm and emission at 810 nm. A calibration curve was established between different ICG concentration and their fluorescence intensity to measure the ICG amount present in the supernatant as shown in Figure 2.5.

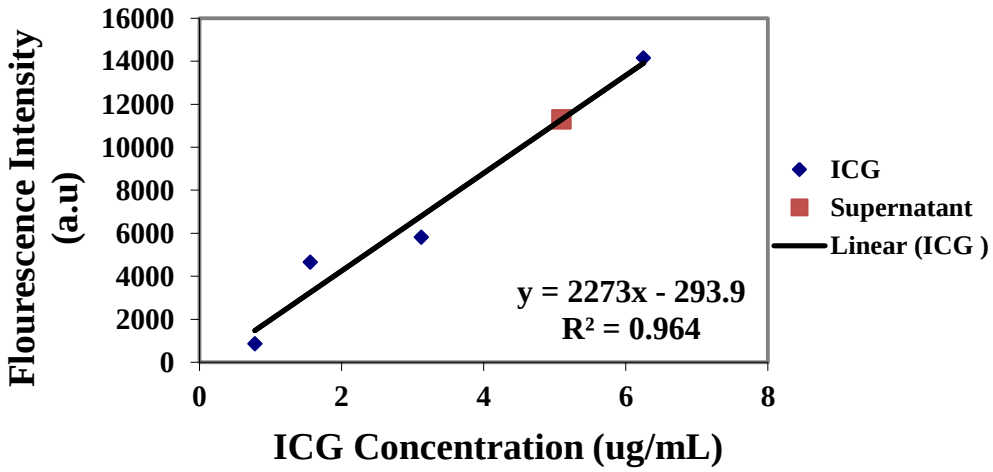

Figure 2.5: Calibration curve for ICG

Figure 2.5 demonstrates a linear relation between ICG concentration and fluorescence intensity with a correlation co-efficient of 0.964. The ICG concentration of the supernatant was then calculated from equation obtained from the calibration curve. The loading efficiency was calculated by an indirect method by using the following formula.

$$\text{ICG Loading Efficiency} = \frac{\text{Amount of ICG used} - \text{Amount of ICG in Supernatant}}{\text{Amount of ICG used}} \times 100\%$$

The amount of ICG used during the formulation as discussed in synthesis process above was 2000 µg/ml. The amount of ICG present in supernatant computed

from the calibration curve was 1009.4 µg/ml. Hence, ICG loading efficiency for PINs calculated from the above equation was found to be 49.5% which represents that almost half of the used ICG was encapsulated in the PINs. I repeated the similar calculations for 3 different batches of nanoparticles and found the mean loading efficiency to be 48.75 ± 5.48% which suggests that encapsulation of ICG within PLGA nanoparticle was relatively consistent.

2.3.3 Excitation Emission Spectra of ICG and PIN

The fluorescence excitation and emission property of PIN and ICG was quantified in 3 different solvents (RPMI media, PBS and DI water) using a spectrofluorometer (RF-5301PC, Shimadzu Scientific Instruments, MD). ICG was thoroughly diluted in the above mentioned solvents respectively to make a final concentration of 20 µg/ml. Similarly, PIN formed were also dispersed completely in above mentioned solvents to have a final concentration of 1 mg/ml. 1 ml of each sample was suspended in a cuvette and diluted 4 times for ICG and once for PIN. The excitation spectra were obtained while scanning from 600-780 nm and by keeping emission wavelength constant at 810nm. Similarly, the emission spectra were scanned from 790-900 nm while keeping excitation wavelength constant at 780 nm. All the measurements were taken at normal room temperature at similar instrumentation.

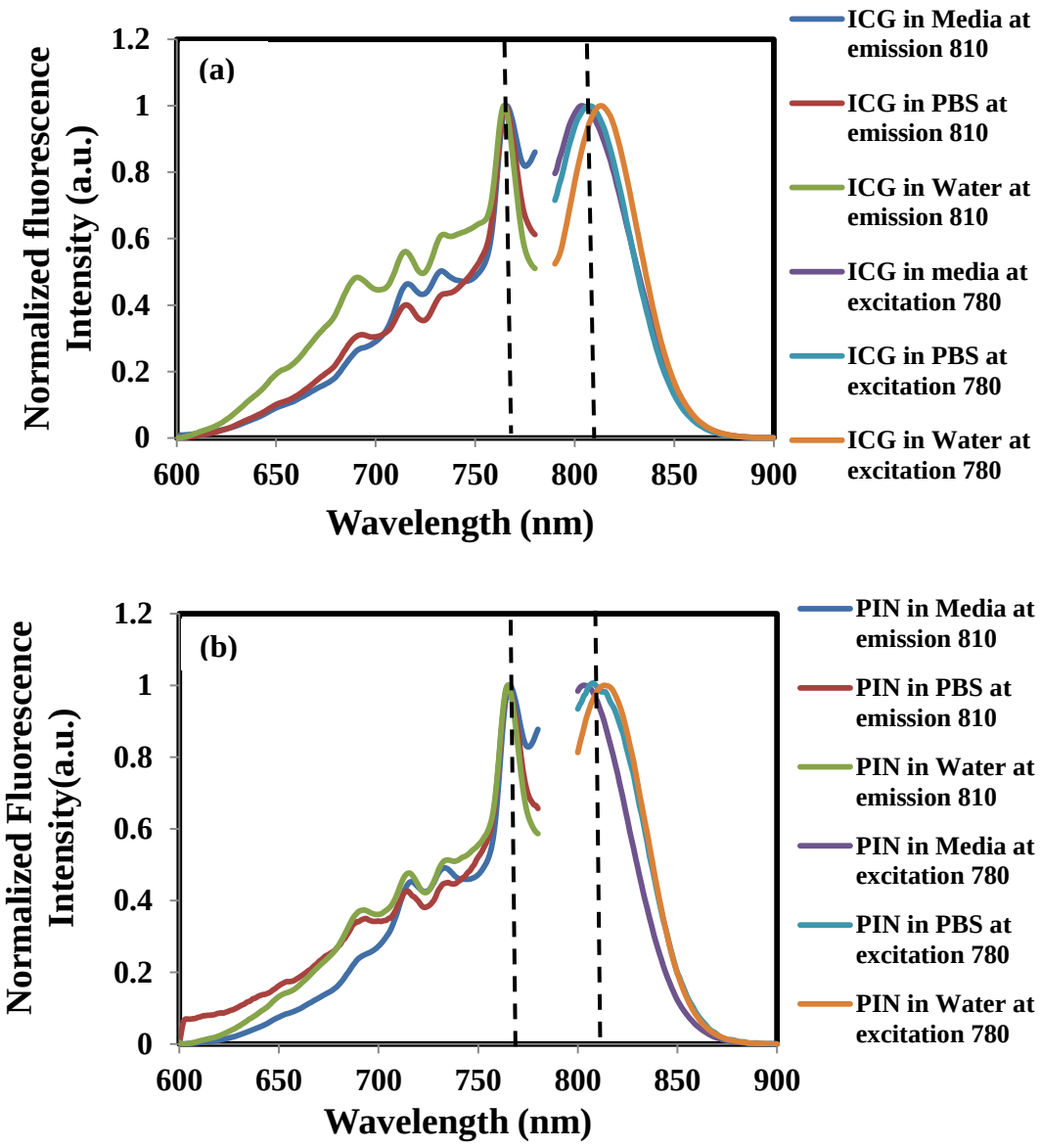

Figure 2.6: (a) The excitation emission spectra of ICG (n=3) in Media, PBS and DI water , (b) The excitation emission spectra of PIN (n=3) in Media, PBS and DI water

Figure 2.6 represents the normalized excitation-emission spectra of ICG and PIN in different solvents. In figure 2.6 (a) and (b), the spectra on the left; from wavelength 600 – 780 nm represents the excitation spectra of ICG and PIN respectively.

Whereas the spectra on the right; from wavelength 790 – 900 nm represents the emission spectra of ICG and PIN. It was observedfrom the plots that ICG and PIN have peak excitation at 765 nm for all of the biorelevant solvents. However, the peak emission for both ICG and PIN shows a ~5 nm shift between solvents. Also, it was observed that the excitation and emission spectra shows similar spectral profile for ICG as well as PIN.

In summay; the excitation spectra for ICG and PIN remains unaffected by solvents, while the emission spectra was influenced slightly within optical limits by different solvents. Also, the results confirm that PLGA conserves the fluorescence spectrum of ICG in PIN (20,29).

2.3.4 Longitudinal Fluorescence Intensity decay study for ICG and PIN

ICG being an amphiphilic dye easily dissolves in water and other solvents. However, ICG shows unstable behavior when dissolved in solvents and degrades with time (25,27). To compare the stability of ICG in various solvents with respect to PIN, the fluorescence intensity of ICG and PIN was quantified at various time periods in different solvents. In addition, the effect of concentration on photostability of ICG and PIN is also evaluated.

Photostability effects in different solvents of ICG and PIN

In order to examine the behavior of ICG and PIN in different solvents, they were dissolved in DI water, PBS and saline to make a final concentration of 50 µg/ml for ICG and 1.5 mg/ml for PIN respectively. 300 µl of sample was taken from these base

solutions and suspended in a well plate to acquire fluorescence measurements. The measurements were taken using a microplate reader at every one hour till 5 hours. In addition, 24, 48 and 72 hour time points were also observed at similar experimental conditions to test the decline of fluorescence intensity for extended period of time. Samples were covered with aluminum foil at room temperature to avoid sample evaporation and photobleaching between measurements. Moreover, at the time of measurement the sample was thoroughly mixed for 2 minutes using a micro pipette to break the aggregated particles. The results of this study are shown in Figure 2.7.

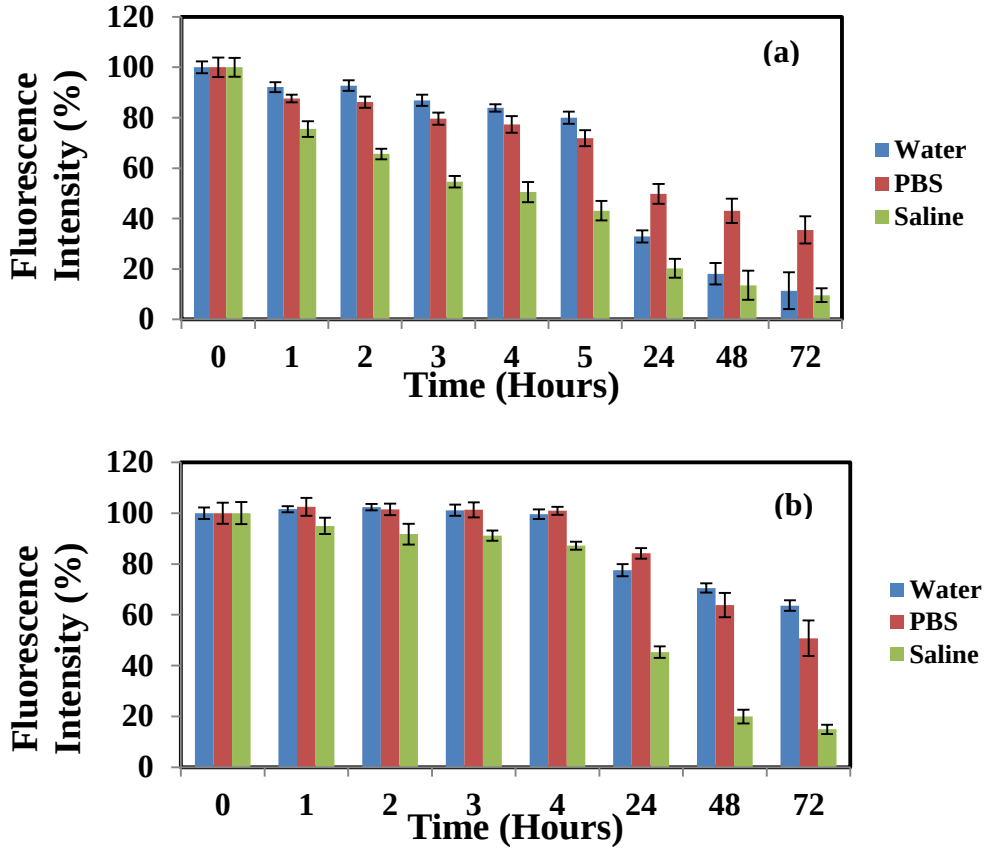

Figure 2.7: Normalized fluorescence intensity with respect to time for (a) ICG (b) PIN for 3 different solvents (DI water, PBS and saline)

Figure 2.7 (a,b) represent the normalized fluorescence of ICG in 3 different solvents over time. The Y- axis represents the normalized percentage fluorescence intensity where the intensity counts at the beginning of the experiment were considered as 100% and the further time points are plotted with respect to the first measurement. As observed from figure 2.7 (a) the fluorescence intensity of ICG in saline reduced by 50% at the end of 4 hour time point whereas for water and PBS the decrease is relatively slower (~20-25%). Whereas in case of PIN in water and PBS, the fluorescence intensity remained unchanged at 4 hour time point and reduction in fluorescence intensity for PIN was ~25%. Also, one can notice from the plot that there was about 20% reduction in intensity after 24 hours for PIN dissolved in PBS as compared to 45% reduction for ICG free dye which signifies its ability to preserve ICG's optical property.

Photostability effects at different concentration of ICG and PIN

To test the fluorescence intensity of ICG and PIN at different concentrations; they were dissolved in DI water to make 3 concentrations (12.5 µg/ml, 25 µg/ml and 37.5 µg/ml for ICG and 1 mg/ml, 2 mg/ml and 3 mg/ml for PIN). The similar instrumentation was employed as described in the previous section to measure the changes in fluorescence intensity of ICG and PIN. 300 µl of sample was taken from these base solutions and suspended in a well plate to acquire fluorescence measurements. The measurements were taken at every one hour till 5 hours at similar experimental conditions to test the decay effect at extensive period of time. Samples were covered with aluminum foil at room temperature to avoid sample evaporation and photobleaching between measurements. Moreover, at the time of measurement the

sample was thoroughly mixed for 2 minutes using a micro pipette to break the aggregated particles. The results of these studies are shown in Figure 2.8.

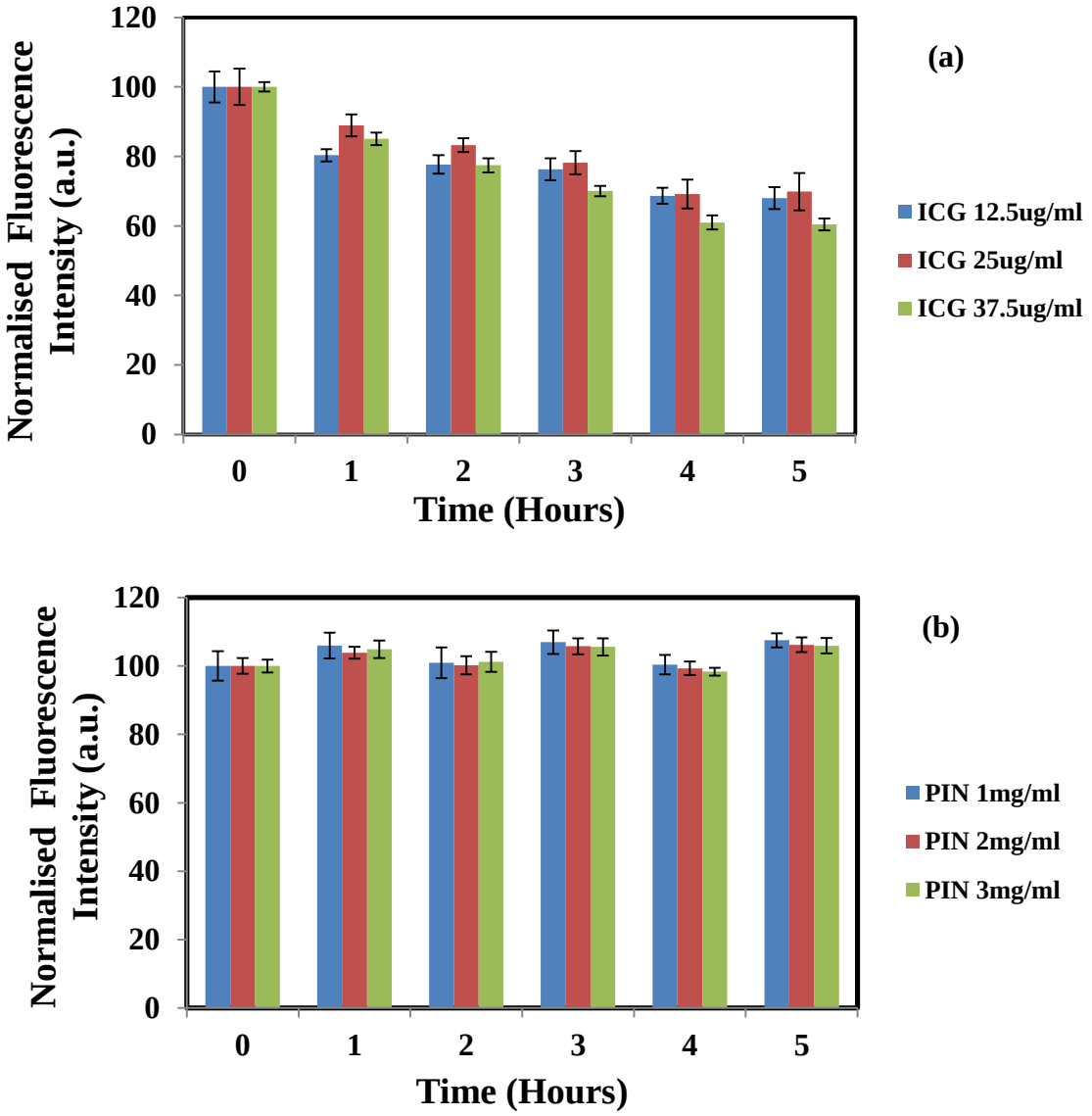

Figure 2.8: Normalized fluorescence intensity with respect to time for (a) ICG and (b) PIN at 3 different concentrations (n=5)

Figure 2.8 represents the normalized fluorescence intensity of ICG and PIN at different concentrations with respect to time. Plots suggest that for all 3 concentrations

the fluorescence intensity of ICG free dye at the end of 5 hours was ~65-75% of the baseline measurement, whereas no change in fluorescence intensity was observed for the same amount of time for PIN. Also, quenching effect was noticed from the plot 2.8 where the highest concentration of PIN and ICG showed lowest intensity (38). These results support the fact that PLGA help preventing the stability of ICG in aqueous solution and also preserves the fluorescence property of ICG (20,29).

2.3.5 Analysis of change in absorption spectra of ICG and PIN as a function of time

A strong absorption of ICG at 780 nm wavelength results into induced hyperthermia for photothermal treatments as well as establishing a significant contrast for DOT and PA (27, 29, 32). However, due to its aqueous instability it degrades over time which in turn affects the absorption properties of ICG (19). In this study, absorption profile and decrease in absorption property for ICG free dye and PIN were evaluated at different time points (0-4 days) with 3 different concentrations.

A spectrometer (Lamda 20, PerkinElmer Inc, CT) was employed to examine the absorption property of ICG. The absorbance was measured between 400 – 900 nm at a step size of 2 nm. To measure the absorption spectra of ICG and PIN at different concentrations; ICG as well as PIN were dissolved in DI water to make 3 concentrations (12.5 µg/ml, 25 µg/ml and 37.5 µg/ml for ICG and 1.15 mg/ml, 2.30 mg/ml and 3.45mg/ml for PIN) 1 ml of sample was then taken from these prepared ICG and PIN solutions and suspended into a cuvette to acquire the absorption spectra. The measurements were taken every day till 5 days at the same experimental conditions.

During the course of the experiment samples were covered with aluminum foil and kept at room temperature. Before each measurement, the samples were mixed thoroughly using a micro pipette to ensure that ICG does not settle down at bottom. The results of absorbance measurements for PIN and ICG are shown in Figure 2.9- 2.11.

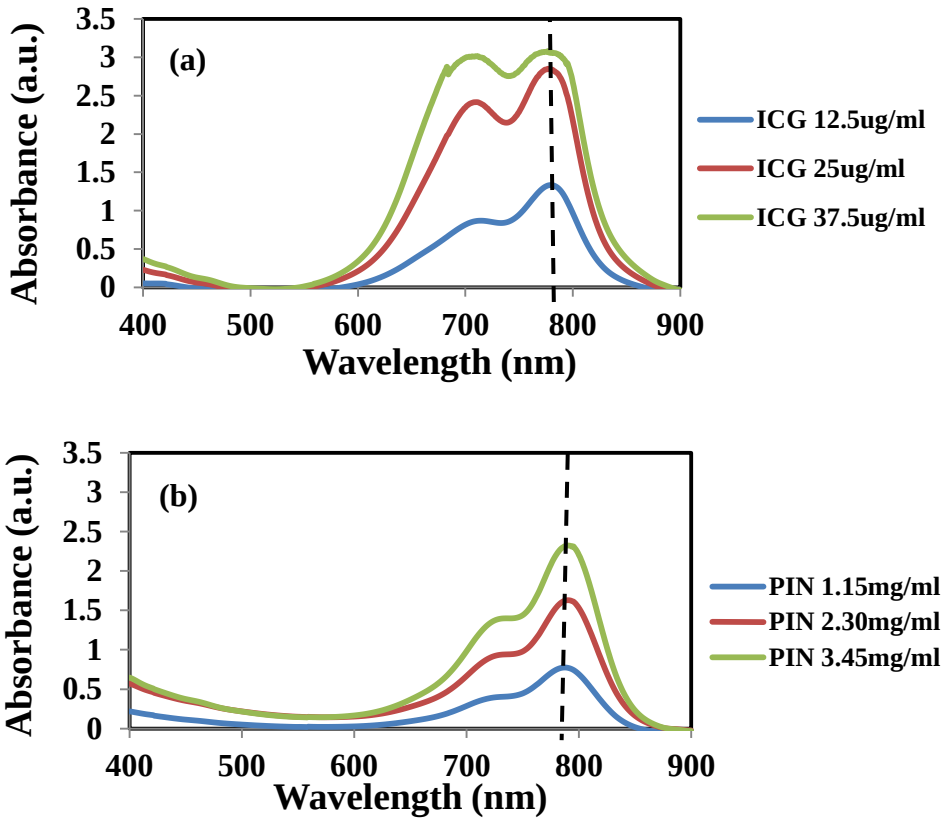

Figure 2.9: The absorption spectra of (a) ICG and (b) PIN at different concentration on Day 1

As observed in Figure 2.9 ICG spectra changes with change in ICG concentration whereas PIN showed no change. The absorbtion spectra changes were due to different arrangement of ICG molecules in an aggregate formation of the ICG dimers (43). Moreover, for every concentration of ICG and PIN, maximum absorbance

was observed at 780 nm. In addition, it was observed that concentration of PIN was 100 fold more than ICG, although the absorbance of PIN is less than ICG which was due to the amount of ICG in PIN . According to the loading efficiency of ICG; the amount of ICG present in 1.15 mg of PIN(with absorbance = 0.74±0.02) was 6.57 µg, which was less than the used 12.5 µg of ICG(with absorbance = 1.3±0.05). Also, PLGA coating on ICG in PIN may reduce the absorbance of PIN.

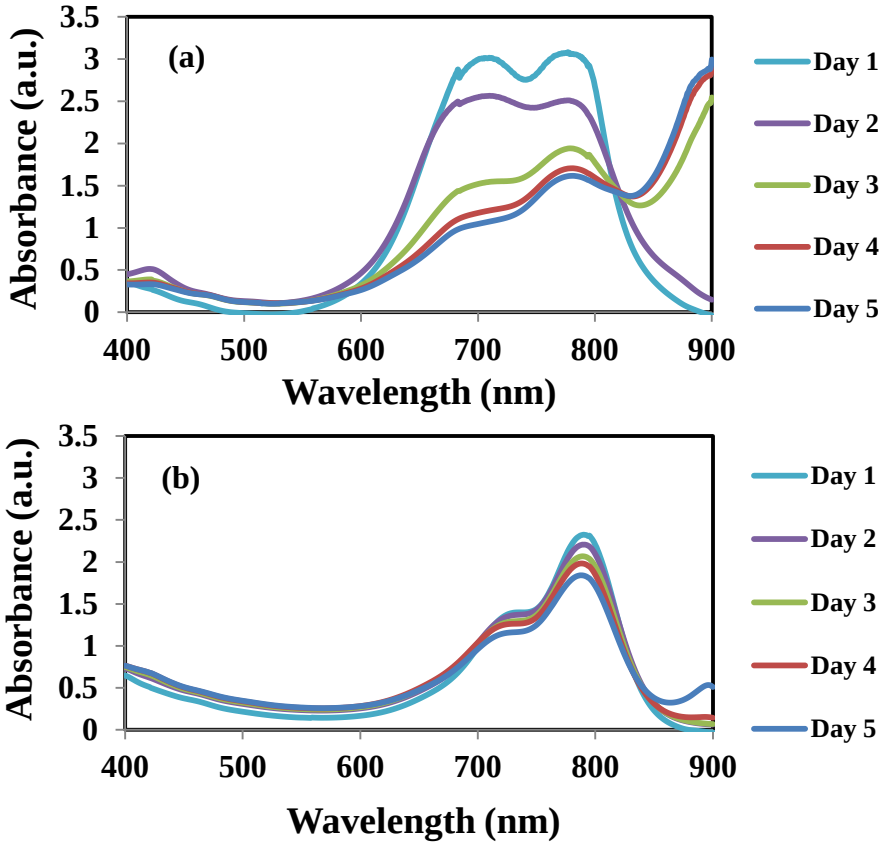

Figure 2.10: The absorption spectra of (a) ICG (37.5µg/ml) and (b) PIN (3.45mg/ml) on different time period

Figure 2.10 shows the absorption spectral changes of ICG and PIN during a time period of 5 days. The change in ICG absorption spectra is due to self aggregation

between ICG monomers which is not found in PIN where ICG monomers are bound to PLGA (29). As observed ICG shows change in absorption spectra after 3 days whereas, no change in spectral characteristic is found for PIN even after 4 days. In addition,the absorbance of ICG decrceases faster as compared to PIN.

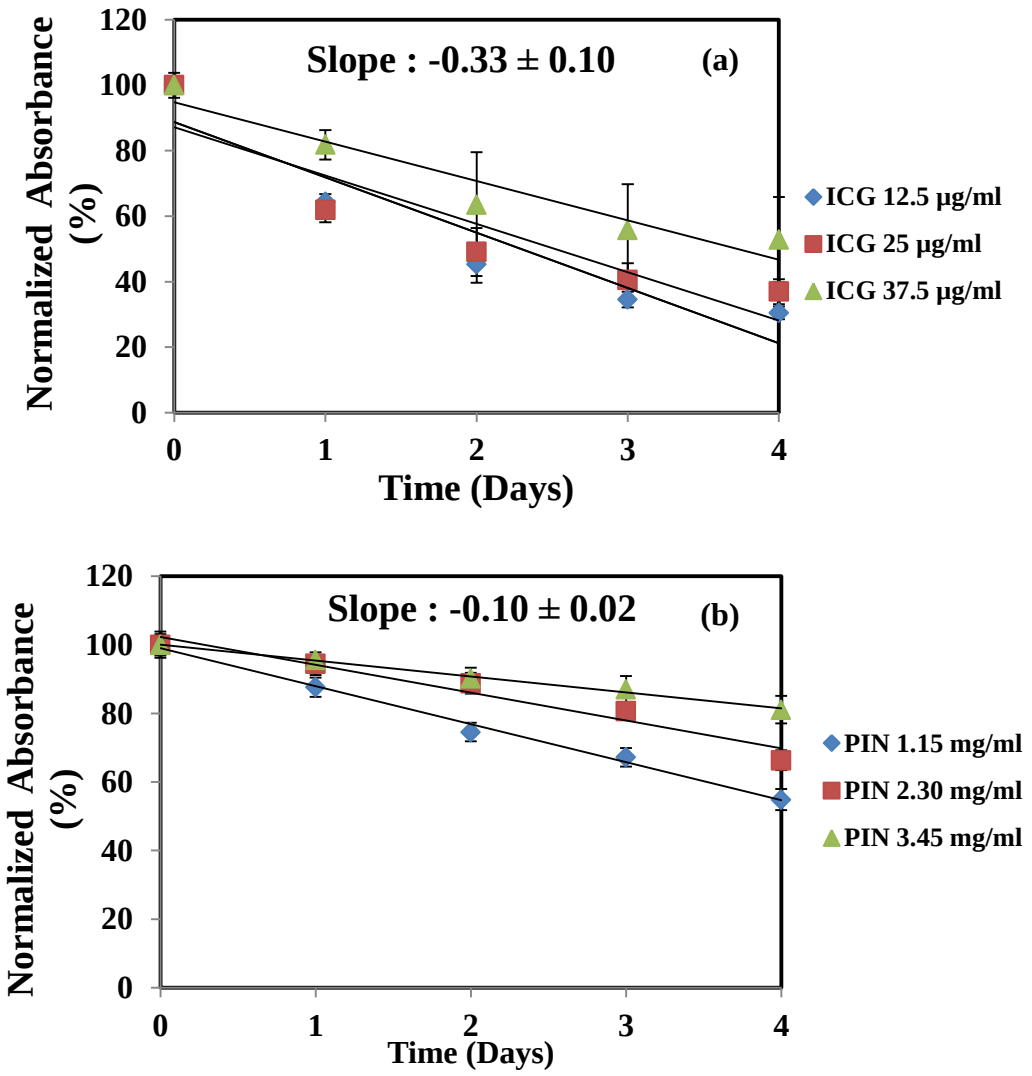

Figure 2.11: Absorbance with time for (a) ICG and (b) PIN at different concentrations

Figure 2.11 represents the decrease in normalized absorbance measurements for ICG and PIN at 3 different concentrations with respect to time. As seen from Figure

2.11 (a, b) the absorbance of ICG at the end of 4 days was decreased by ~60% for all the concentrations from initial measurement, whereas for PIN decrease was ~20%. In addition, it was observed that all the three concentration of ICG and PIN solution showed similar decay pattern. Moreover, the slope of fluorescence decay was calculated by fitting a linear regression for each concentration of ICG and PIN. The mean slope for ICG was 0.33±0.1 whereas for PIN it was 0.1±0.02. Thus, PLGA not only preserves absorption property of ICG in PIN but reduces the decay rate (29,20).

2.3.6 Effect of different concentration of ICG and PIN on Fluorescence lifetime

Fluorescence lifetime is the time taken by the fluorophore to remain in the excited state. It generally depends on the structure of the fluorophore, and environmental parameters like pH, temperature and oxygen concentration (36,37). In this study, the relation between fluorescence lifetime and fluorescence intensity (fluorophore concentration) is quantified which is an important parameter for future lifetime imaging applications.

Initially, ICG was dissolved in DI water to make final concentrations of 25 µg/ml, 50 µg/ml and 75 µg/ml. Further, PIN was dissolved in DI water to make final concentrations of 5 mg/ml, 7.5 mg/ml and 10 mg/ml. 300 µl of sample was taken from these prepared solutions and suspended in a well plate to acquire time resolve fluorescence images. A time gated ultrafast Intensified CCD (ICCD) camera was employed to measure the fluorescence intensity and fluorescence lifetime. Samples were excited with a 50 picosecond (ps) broadband pulsed laser (SC-450, Fianium Inc.,

Eugene, Oregon) filtered by a 780 ± 10 nm excitation filter. Emitted light was filtered by an 820 ± 10 nm emission filter. Images were captured at every 0.05 ns for a period of 5 ns by the ICCD camera. Moreover the system response function was measured by irradiating a white sample and acquiring the reflectance of it from the images captured at every 0.05 ns for a period of 2.5 ns. The images once acquired were analyzed for fluorescence intensity and lifetime measurement using MATLAB (Mathworks Inc., Natick, Massachusetts) software. The results of the intensity and lifetime measurement are shown in Figure 2.12, 2.13 and 2.14.

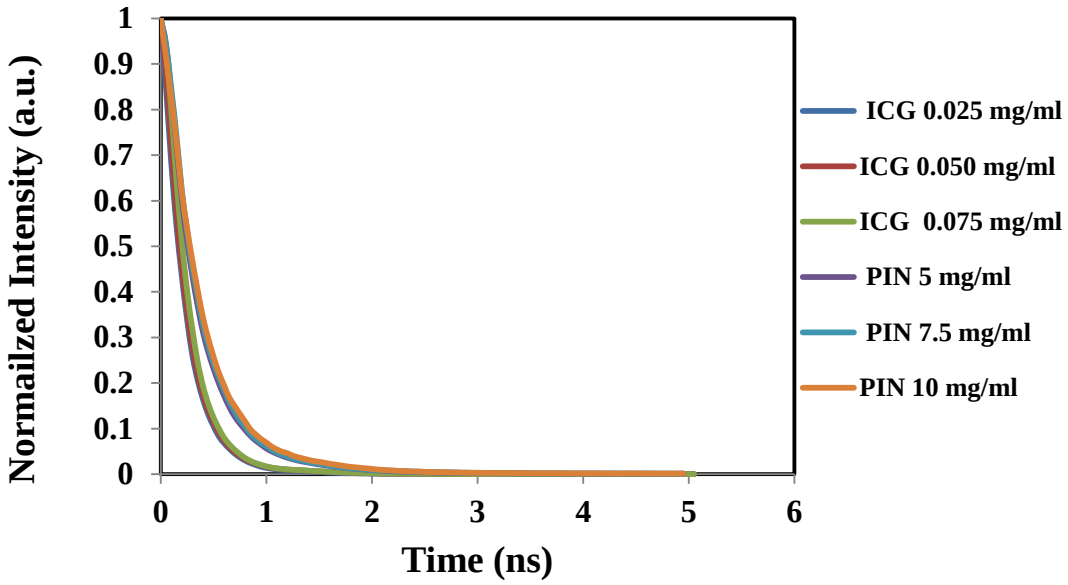

Figure 2.12: Normalized fluorescence decay curve for ICG and PIN

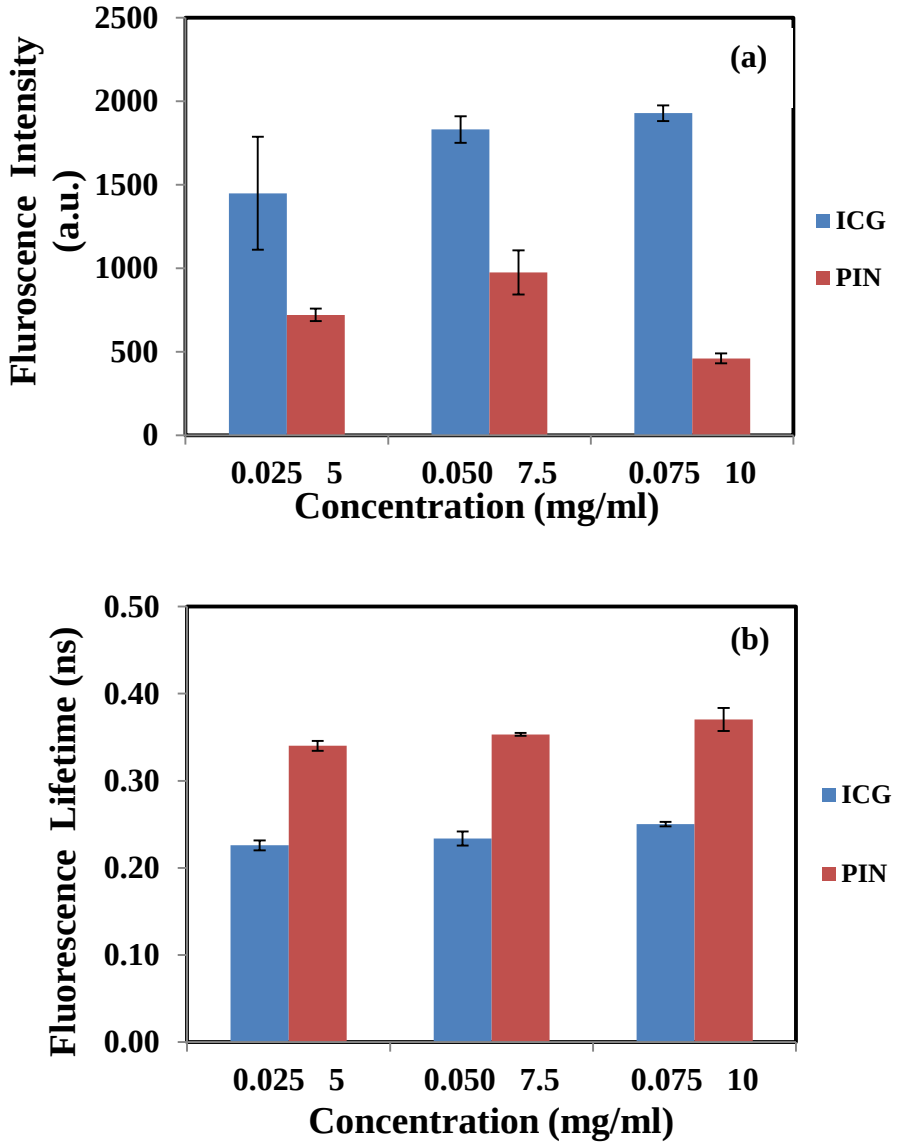

Figure 2.13: (a) Comparison of fluorescence intensity and (b) comparison of fluorescence lifetime for ICG free dye and PIN

Figure 2.12 represents normalized fluorescence decay profiles for 3 different concentrations of PIN and ICG. It was observed that the PIN takes a longer time to decay as compared to ICG which was expected as PLGA shell prevents excited ICG molecules to return back to the ground state. The flourescence intensity of ICG and PIN

at various concentrations are shown in figure 2.13 (a). It was observed that there is a significant change in intensity with the change in concentration of PIN and ICG. Also, for PIN the intensity for 20 mg/ml concentration is lower than the other two which are at 10 mg/ml and 15 mg/ml PIN concentrations. This can be explained by fluorescence quenching phenomenon which causes decrease in intensity at higher fluorophore concentrations (38). In figure 2.13(b) the lifetime of ICG and PIN are demonstated for different concentrations. As fluoroscent lifetime represents the time period during which a fluorophore remains in the excited state and it is independent on flourophore concentration; there is negligible change in lifetime with the change in concentration of ICG and PIN. Also, the lifetime of PIN (0.35 ns) is found to be greater than that of ICG (0.24 ns) due to PLGA. In addition,the measured lifetime of ICG was found different than the published lifetime of ICG. Hence, the affect of the system response on lifetime of ICG and PIN was studied.

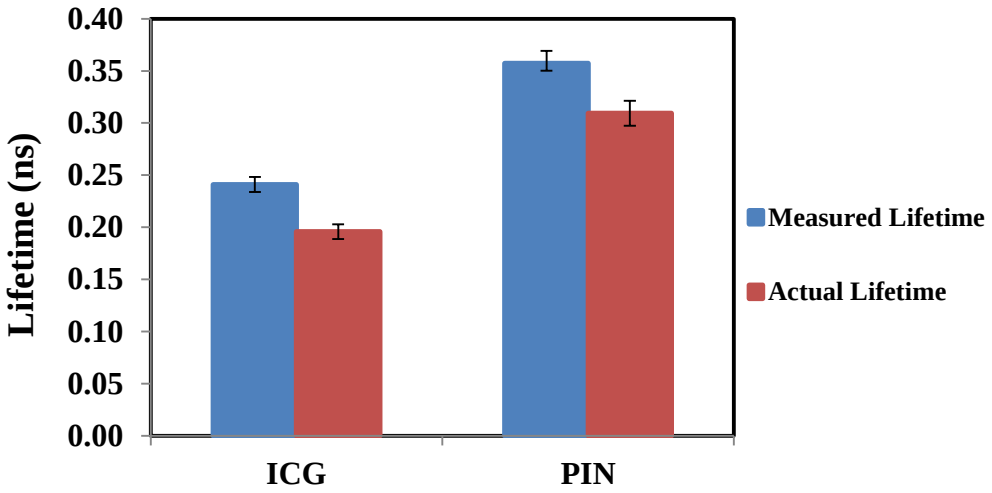

Figure 2.14: Comparison of measured fluorescence lifetime and actual lifetime obtained for ICG free dye and PIN

In order to measure the actual lifetime of ICG, the response function obtained from white sample was deconvoluted with the obtained ICG fluorescence decay curve. The resultant deconvoluted curve was further fitted to obtain the pure lifetime value. Figure 2.14 represents the measured and actual lifetime of ICG and PIN. It was observed that the measured lifetime of ICG and PIN which were 0.24 ± 0.01 and 0.35 ± 0.01 ns respsectively were decreased to 0.19 ± 0.01 and 0.30 ± 0.01 ns respectively after deconvolving the system response function. Moreover, the obtained actual lifetime of ICG was close to published lifetime values of 0.17 ns (36,37). Also, gate width of the camera is a limiting factor that affected lifetime values. The simillar value as published in literature can be achieved by reducing the gate width with advanced instrumentation in future.

2.3.7 Cytocompatibility study of PIN

Biocompatibility study was performed to evaluate the toxicity of PIN at 6 hours and 24 hours. Human dermal Fibroblast cells (HDF) were cultured in complete Dulbecco's Modified Eagle Medium (DMEM) supplemented with 10% serum and 1% penicillin-streptomycin and maintained at 37°C, 5% CO_2 in humid atmosphere of an incubator. Once the cells reached 80-90% confluency, they were passaged and seeded at a density of 5000 cells/well in two 96-well plate and allowed to attach overnight. Nanoparticle suspensions were made in various known concentrations (0, 0.1, 0.25, 0.3, 0.5, 1, 2.5 and 5 mg/mL) and added to the cells. The cells were further incubated at 37°C, 5% CO_2 for 6 hours and 24 hours respectively. At the end of the incubation time,

the nanoparticle suspensions were removed, and the cells were supplemented with complete DMEM media to which 20 µL of MTS reagent was added. The cells were incubated with the MTS reagent for 2 hours, and then absorbance measurements were taken at 490 nm to determine cell survival. Cells exposed to complete media without any nanoparticles served as control samples. In addition to that the nanoparticle suspension was added to blank well plates without any cell for background measurements. The results are shown in Figure 2.15.

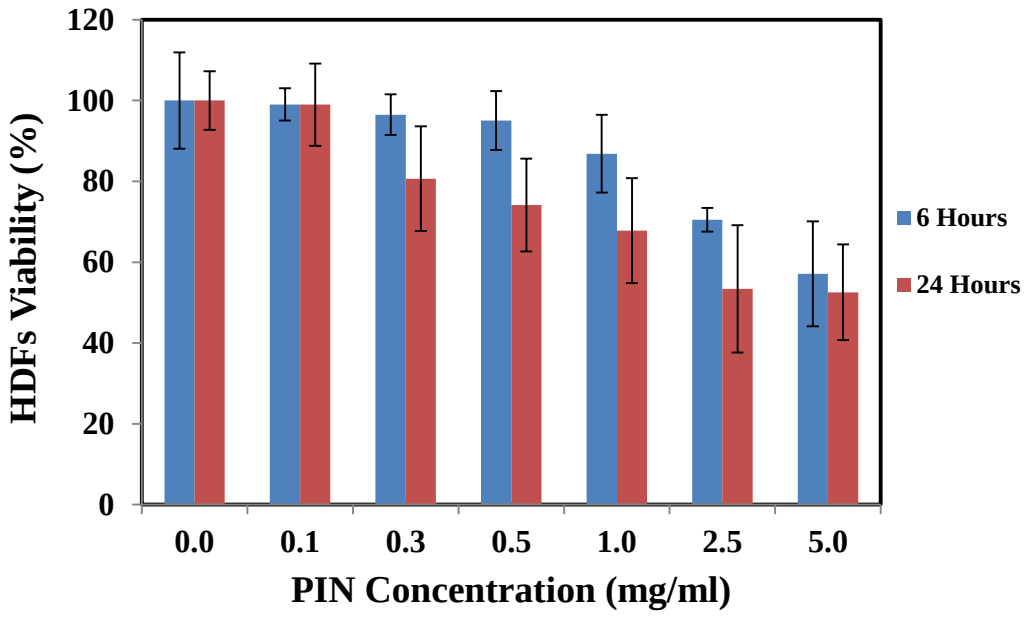

Figure 2.15: Cell viability study of PIN at 6 and 24 hours

As shown in figure 2.15, the cell viability was obtained by absorbance measurements from the incubated cells after 6 hours and 24 hours. After 6 hours it shows a significant cell viability of 85% till 1 mg/ml nanoparticle concentration. In case of the 24 hour study, the cell viability was significant till 0.5 mg/ml. The cell viability for higher concentrations did not show any significant difference with the control.

Hence, PIN are biocompatible with the healthy cells for lower concentrations and have shown no toxic effects.

2.4 Cellular Uptake Study

2.4.1 Introduction

The nanoparticles were investigated for their targeting ability by a cellular uptake study. Various antibodies such as aptamers, integrins and folic acid have been used to target prostate cancer (44). In this study the nanoparticles were conjugated with three different peptides; (i) RGD-4C peptide that targets the tumor vasculature, (ii) Folic acid that targets the folate receptors on surfaces of tumor cells and (iii) R11 peptide that targets prostate cancer cells. The previous studies by J. Zhou et al. have shown that R11 peptide has a greater affinity for prostate cancer cells (45). Hence, nanoparticles were conjugated with, RGD-4C, Folic acid and R11 peptide to evaluate the cellular uptake of conjugated nanoparticles on prostate cancer cells.

2.4.2 Conjugation of PIN with R11 peptide, RGD-4C peptide and Folic acid (FA)

For conjugation, 10 mg PIN were suspended in 1 ml of PBS. The nanoparticle suspension was further activated by 200 mM of NHS and 400 mM of EDC and the reaction were carried out for 1 hour on an orbital shaker at room temperature. The resulting NHS activated PIN were covalently bonded with 1 µM of RGD-4C, R11 and Folic acid and mixed thoroughly by a mechanical vortex machine and further reaction

was continued for 12 hour on an orbital shaker at room temperature. The conjugated PINS were then stored at -20°C in a freezer (46,47).

2.4.3 Cellular binding and uptake of PIN by PC3 cells

Prostate cancer – PC3 cells were cultured in RPMI media and were allowed to grow till confluency. Once they reach the confluency the cells were seeded in 96 – wells plate at a density of 12000 cells/well and placed in the incubator for 24 hours and allowed to grow. The conjugated PIN and non-conjugated PIN solutions of known concentration (50,100, 200, 300, 500 and 1000 µg/ml) prepared in RPMI media were added to the cells and incubated for 2 hours. After 2 hours of incubation the media was removed and the cells were washed thrice with PBS. 300 µl of triton was added in each well to kill the cells. After 15 minutes the cells were scrapped from the surfaces and 200 µl of cells suspension were filled in vials.

The nanoparticles uptaken by cells were analyzed by fluorescence measurements. 100 µl of cell suspension from the vials were suspended in well plates and the fluorescence intensity was measured using a spectrophotometer (Infinite M200, TECAN group Ltd., Switzerland) at 780 nm excitation and 810 nm emission. The cell suspensions in the well plates were further analyzed for the total DNA content by a Pico green DNA assay. The assay was performed using the Pico green DNA assay kit according to the instructions in the manual. The ICG characterization curve was used to calculate the ICG amount present in the nanoparticles. The cellular uptake results were

computed from the fluorescence intensity of ICG present in nanoparticles and normalized with the DNA content per sample.

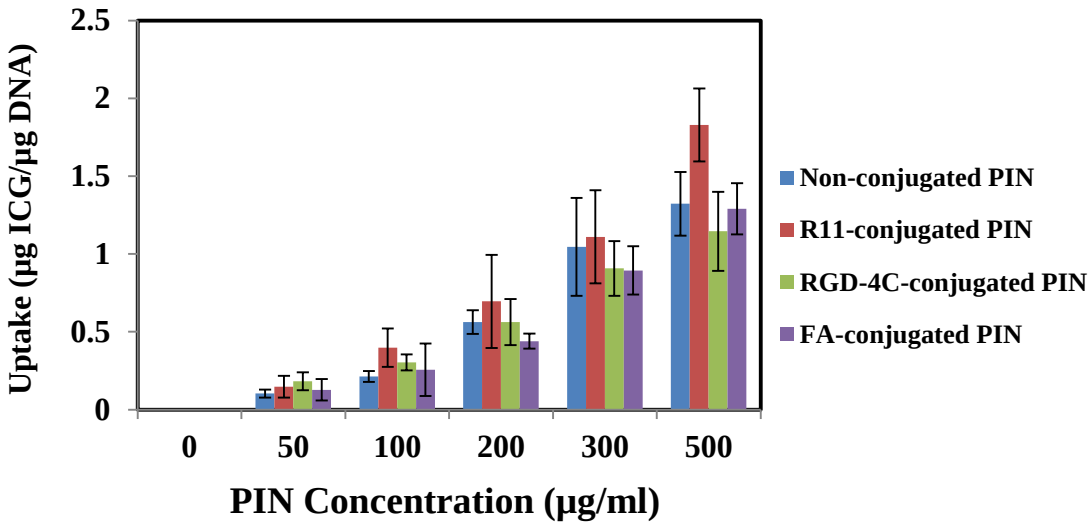

Figure 2.16: Cellular uptake of non conjugated PIN and PIN conjugated with R11, RGD-4C and Folic Acid (FA)

The results indicate a significant uptake by R11 conjugated nanoparticles as compared to non conjugated and conjugated nanoparticles with RGD-4C and Folic acid as shown in figure 2.16. Also, the uptake shows more significance at higher concentreation.Hence R11 peptide shows strong ability of targetting prostate cancer as compared to RGD-4C and folic acid.

CHAPTER 3

THERAPEUTIC APPLICATIONS OF PIN AS THERMAL AGENT

3.1 Background

Photothermal therapy involves light interaction with tissue under appropriate condition to raise the temperature above 42˚C leading to cellular destruction (40). Since tumor tissue is more sensitive to temperature, this temperature raise is sufficient to induce cell death in tumor tissue than normal (42). Hence, this application for cancer treatment has gained interest as compared to the conventional methods due to its noninvasive approach (40,42). However, the chromophores in the healthy tissue in the expossed light path also absorb this light which in turn reduce heat deposition in cancer cells and increase nonspecific injury to the surrounding healthy tissue (39). This can be overcome by employing target specific exogenous thermal agents which can absorb specific wavelength light and release heat to the tissue of interest. In order to achive deep tissue penetration NIR light is being used (19,29,30). Dyes that strongly absorb NIR light increases the heat deposition in cancer cell allowing selective killing of tumor cells.

Recently, gold nanoparticles and carbon nanotubes have received much attention for hyperthermal treatments because of strong absorption of NIR light and strong photostability (39). Although the main drawback is minimal biocompatibility,

which makes them toxic and hence they need to be coated with a biocompatible material (41). Whereas, ICG and PLGA are biocompatible and biodegradable, along with that ICG has shown a strong absorption in the NIR range (780 nm) and also, PLGA conserves the photostability of ICG (Chapter 2). This advantages support the use of PIN for photothermal treatment for cancer.

In this study I have verified the potential of PIN for photothermal therapy using intralipid gelatin tissuelike phantom and chicken breast phantom.

3.1.1 Instrumentation

I employed a single Fiber Array Package (FAP) Laser system to induce heat in the phantom, where the temperature rise was continously monitered by a Data logger through thermocople wires. Following sections briefly discribes the instrumentation.

FAP Laser System

The FAP System (Coherent Inc., Santa Clara, CA) is a continuous wave system emitting light at 808 nm wavelength. It has a power output up to 30W of diode light into an armored 800 μm core fiber and a NA of 0.22. The optical fiber is 3.5 metres long and is terminated to the SMA- 95 connector. This fiber transmits the laser energy in a forward direction and which is coupled with armored optical transport fiber using a connector. The system is rack-mountable and can be controlled either by the front panel user interface, or by a computer-controlled RS-232 interface (48).

Figure 3.1: Single FAP laser system

Data Logger

The Fluke Hydra 2625A data logger (Kandel Electronics, Oreland, PA) as shown in Figure 3.2 is a 21-channel data logging instrument that holds 2072 memory sets for each channel. It is capable to take scans every seconds and continuously take up to 24 hours. The data logger measures as well as records temperature via thermocouples from multiple measurement locations. Also, thermocouple reference junction compensation is automatically performed by sensing the temperature of the input module's isothermal block (49).

Figure 3.2: Fluke Hydra data logger

The data logger was connected to the Hydra data logger software in the PC through an RS-232 serial interface for real-time data acquisition. This data logger also has removable memory data storage, internal memory storage, and direct real-time data transfer options. Also, the removable Universal Input Module enables fast, convenient set-up and reconfiguration. The Hydra data logger is ideal for recording data during environmental stress screening, thermal testing, design testing, and other applications that require data logger with up to twenty analog measurement channels (49).

Thermocouple

A high quality T-type themocouple (Omega Engineering Inc., Stamford, CT) made from copper and constantan was used for temperature mesaurements. These thermocouples can measure temperature from -200 to 350 °C range (50). The thermocouple were soldered to the universal input module of the data logger measurements.

3.1.2 System calibration

The laser power meter (Field MaxII, Coherent, CA) was used for power measurement. These meter functions with a broad range of thermopile and optical sensors. These sensors enable to measure UV, visible, and IR laser output of pulsed lasers. It is able to measure power from 3 mW to 30 kW range (48).

In order to measure the output power of the laser, the power meter was turned ON and the background power reading was taken. The laser tip was further held in the center of the optical sensor and the laser was the turned ON and the power was monitored. The

laser power was found to be 0.8 W for 8 A laser current which is optimum for hyperthermia treatments.

Temperature measurements from different channels of data logger

It was important to test data logger system performance and stability before phantom experiment. Therefore, temperature measurements from two data logger channels were compared with a measurement taken with a single channel thermometer (HH508, Omega Technologies Inc., CT).

For calibration, a glass beaker filled with cold tap water was placed on a heating plate, while it was continuously stirred with a magnetic stirrer for uniform distribution of heat. The thermocouple needle as well as thermocouple wires connected to the two channels of data logger were inserted in the beaker such that all three were dipped in water as shown in figure 3.3. The temperature was continuously monitored after every 5 seconds till 10 minutes from both the systems. The results are presented in figure 3.4.

The plot in figure 3.4 represents the simultaneous temperature measurement from two data logger channels and the thermometer over 500 seconds. It was noticed from the plot that there exists no difference in measurements for the two channels of the data logger. Also, data logger-thermo couple assembly behaved same as the digital thermometer and thus can be used for reliable temperature measurement during phantom measurements.

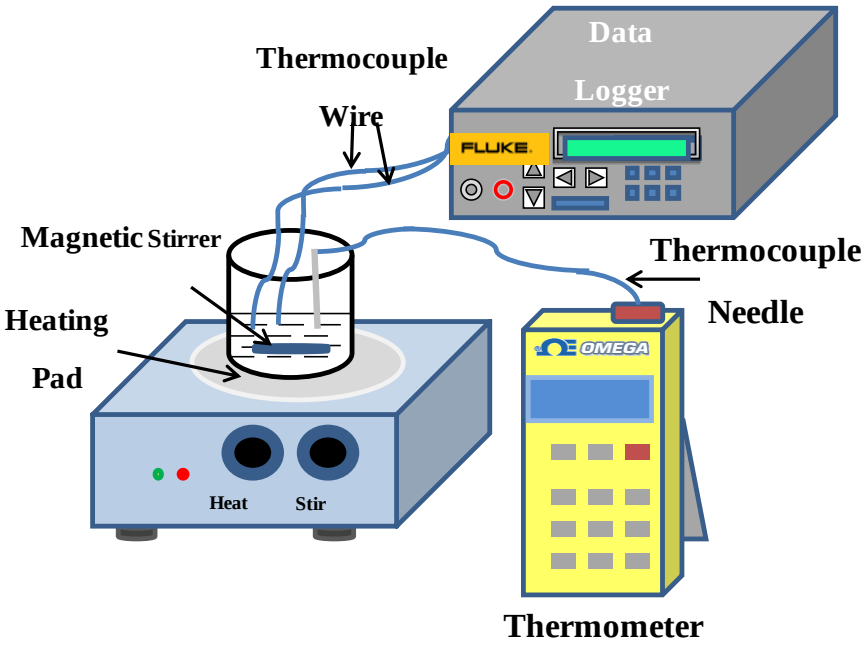

Figure 3.3: Experimental setup for the calibration of the data logger system

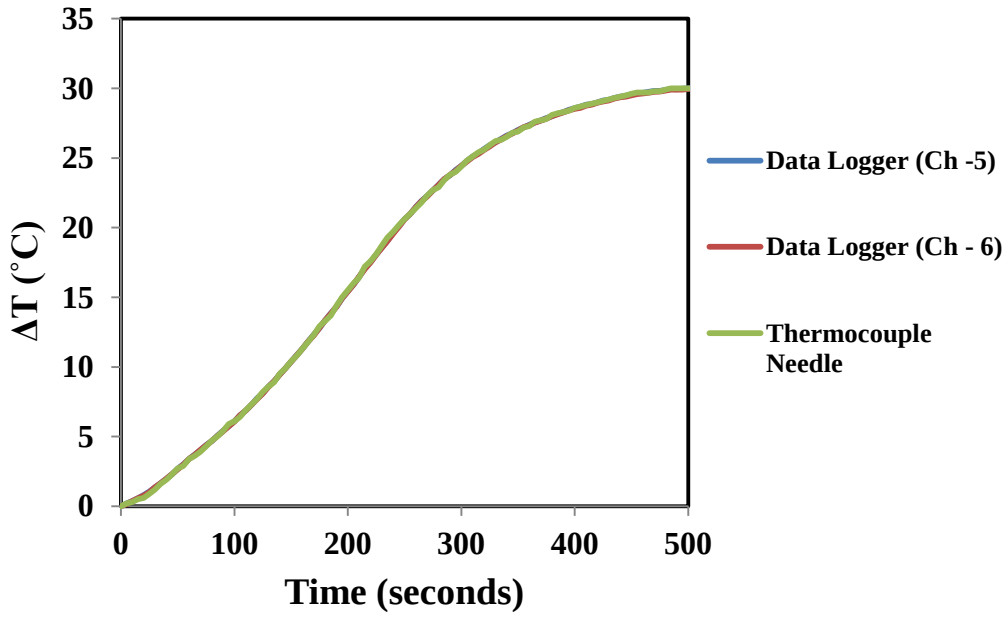

Figure 3.4: Temperature profile from two channels of data logger and the thermometer

3.1.3 Preparation of phantom

Phantom is a tissue simulating material that mimics optical properties of human or animal tissue at different wavelengths (51, 42). I developed such tissue-like phantoms to study thermal ablation ability of PIN and ICG. Three types of phantom were prepared for this study as described below:

(i) Control phantom – Intralipid gelatin phantom

(ii) ICG phantom – ICG based intralipid gelatin phantom

(iii) PIN phantom – PIN based intralipid gelatin phantom

Materials and Method

I used 20% intralipid (Baxter Inc., Deerfield, IL) - a sterile, non-pyrogenic fat emulsion made up from 20% soybean oil, 1.2% egg yolk phospholipids, 2.25% glycerin, water (51), gelatin powder (Type – A, Sigma Aldrich, MO) – a heterogeneous mixture of water-soluble proteins of high average molecular weights (52), paraformaldehyde and water for phantom preparation.

In the beginning 2 solutions were prepared: (1) ICG (0.1 mg, 0.3 mg and 0.5mg) in 2 ml intralipid (20%) and (2) PIN (25 mg, 40 mg and 55 mg) in 2 ml intralipid (20%). Also, 25 mg Paraformaldehyde was added to each of these solutions to achieve higher melting point for phantoms during laser irradiation. Thereafter, 2 grams of gelatin powder in small portions was added into 10 ml of boiling water. The gelatin solution was vigorously stirred until it was homogenously mixed and making sure that

no clumps was formed. Once gelatin was completely dissolved in water, it was cool down to 45 °C and bubbles were removed before adding prepared intralipid solutions (1, 2 or 3) into it. Finally, the prepared mixtures of 2 ml intralipid were homogenously mixed with it. This mixture was transferred in a 10 ml glass beaker (2.5 cm dia., 3.0 cm height) to form a cylindrical phantom. The molds were refrigerated at 4°C for about an hour and then the phantoms were taken out from the mold for further phantom measurements. In addition, a control was made without PIN/ICG using the same synthesis process to compare the results for thermal ablation phantom study. The prepared control, PIN (2.08, 3.33 and 4.58 mg/ml) and ICG (0.008, 0.025, 0.041 mg/ml) phantoms are shown in figure 3.5.

Moreover, for the chicken breast phantom study; the phantoms were prepared in a well plate to form small cylindrical molds (0.5 cm dia., 0.75 cm height) using the same process.

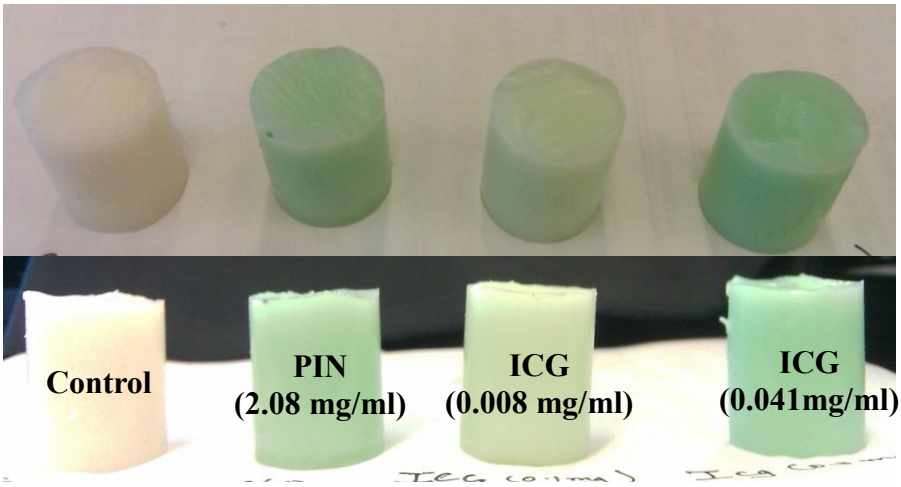

Figure 3.5: Top views and side view of Control, PIN and ICG tissue-phantom

3.2 Intralipid Gelatin Phantom Study

In this study I used previously described intralipid gelatin phantoms with ICG and PIN to evaluate their ability to induce local hyperthermia. ICG being a strong absorber, releases heat when irradiated by NIR light. PIN has shown similar optical characteristics as that of ICG (Chapter 2), moreover it is more stable than ICG. Hence, the objective of this study is to investigate the capability of PIN and ICG based tissue-like phantom as thermal therapy agent instead of using conventional gold nanoshells to induce local heating (39). Control phantom (without ICG/PIN) mimics the simulating tissue model with tumor whereas the ICG and PIN phantoms simulate the tumor tissue homogenously introduced with exogenous chromophore. In this study, temperature change of all the three types of phantoms were examined at different depths and distances.

3.2.1 Experimental Setup

I used an 808 nm continuous wave diode laser (Coherent Inc., Santa Clara, CA) to irradiate the phantoms. The experimental setup is shown in figure 3.6. The laser tip was set perpendicularly on the top surface of the phantom. The tip lay in the center and 1 mm away from the top surface of the phantom. All the thermometers wires had a 2 mm of non-insulated tip. Three thermocouple wires were inserted perpendicularly on the top; separated by 3 mm, 5 mm and 7 mm from the laser tip for distance measurements. Similarly, three thermocouple wires were inserted perpendicularly on

the side of the phantom such that the non-insulated tip of the thermocouple lay in the center of the phantom and also the wires were separated by 3 mm, 5 mm and 7 mm from the top surface of the phantom. The thermocouple wires were connected with different channels of the data logger. The data logger was connected to a PC through a RS – 232 serial port.

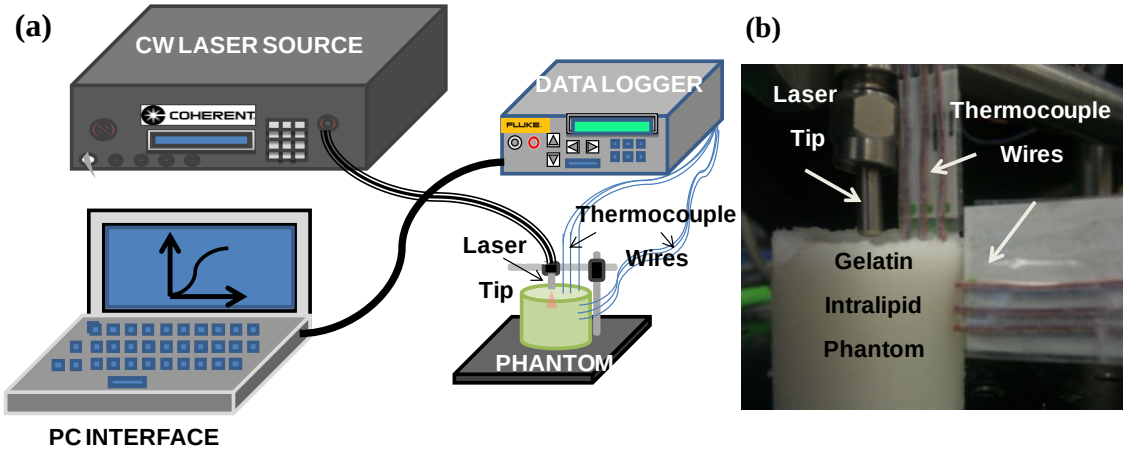

Figure 3.6: (a) Schematic of the experimental setup (b) Actual experimental setup

3.2.2 Data Acquisition

After initial setup, data logger and the PC were turned ON. Using hydra software the channels in use were initialized and also the thermocouple type was set as T-type. Also, data scanning time was set at 5 seconds. Thereafter, phantom temperature homogeneity was tested by reading all the connected channels of the data logger. After confirming temperature homogeneity the laser system was enabled with 8 A current which resulted in 0.8 W irradiation power.

The data acquisition was started by clicking on the run tab on the hydra software. The first few measurements were taken while keeping the laser OFF for 30 seconds to get a few baseline measurements which showed the temperature of the phantom at room temperature. After 30 seconds, the laser was turned ON and the temperature measurements were continuously monitored for each thermocouple location for every 5 seconds till 5 minutes. After 5 minutes, the laser was turned off and the acquisition was stopped. The data were saved as excel file with the time and temperature measurements from each channel. The same experiment procedure was performed on all the phantoms for distance and depth temperature measurements. The data was further analyzed and the results are explained in the next section.

3.2.3 Results and Discussion

Once the data acquisition was done the results were analyzed in excel. In order to determine the actual temperature difference the change in temperature was calculated by subtracting the final temperature value from the initial temperature value when the laser was switched ON.

The temperature difference after 5 minutes of laser irradiation are plotted for the control, ICG and PIN phantoms for all the depths and distances as shown in Figure 3.7 and Figure 3.8.

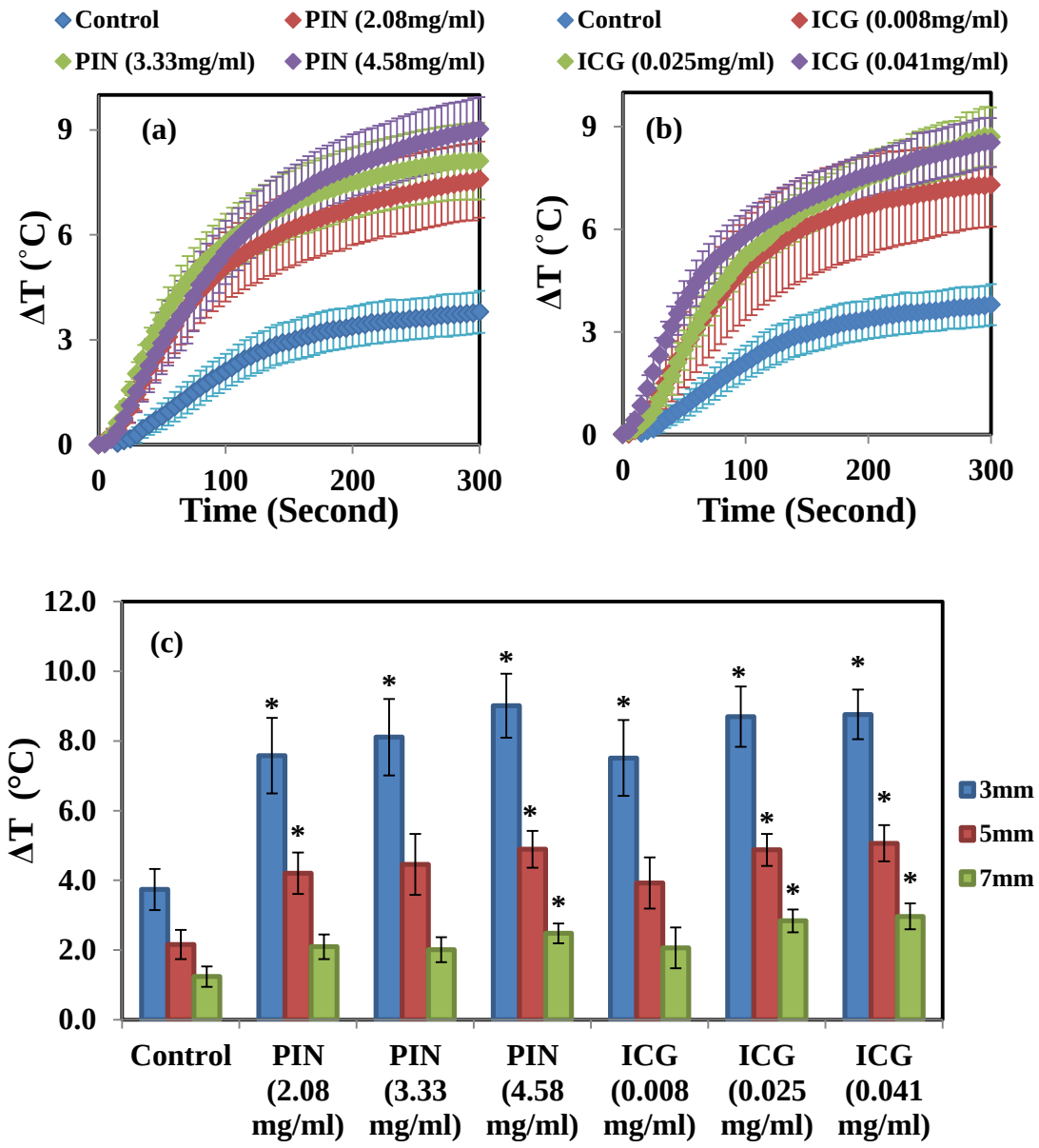

Figure 3.7: Temperature profile with respect to time at 3 mm distance from laser for (a) PIN and (b) ICG, (c) Peak change in temperature at 3, 5 and 7 mm distances for Control, PIN and ICG phantoms

Figure 3.7 (a,b) shows, the temperature profile of control, PIN and ICG phantoms with respect to time measured at 3 mm distance from the laser tip. At the

beginning a sharp increase in temperature was found within 60 seconds which gradually increases with time and finally reaches a plateau. As observed, control phantom shows a small change in temperature (~2°C) after laser irradiation whereas PIN and ICG phantom have shown a greater change (~8-10 °C). This demonstrates the efficiency of ICG to release heat on absorption of NIR light. Moreover, ICG and PIN shows identical temperature profile which signifies that PIN has similar heating capability as ICG. Further, the plot suggests that the higher concentration of ICG gained greater temperature which can be obtained in case of PIN also. In addition, figure 3.7 (c) shows the peak temperature change achieved after irradiating the phantom for 5 minutes for all the phantoms at 3 mm, 5 mm and 7 mm distance. A gradual decrease in temperature was observed with increasing the distance from 3 mm to 7 mm for all phantoms. This signifies a uniform distribution of heat achieved in the area near by laser tip as compared to the surrounding area of the phantom. As seen in Figure 3.7 (c) the temperature change for ICG and PIN phantoms for all the three concentration is ~2 times more than that of control phantom. At 3 mm distance, peak ΔT achieved for ICG (0.041, 0.025 and 0.008 mg/ml) was 8.8 ± 0.7˚C, 8.7 ± 0.8˚C and 7.5 ± 1.08˚C respectively whereas for PIN (2.08, 3.33 and 4.58 mg/ml) the same was 9.0 ± 0.91˚C, 8.1 ± 1.09˚C and 7.8 ± 0.6˚C respectively which can induce local hyperthermia (42).

Moreover, it was observed from figure 3.7 (a,b,c) that the concentration of ICG used was 200 folds less than PIN, but the similar heating effect was achieved from the two phantom. As discussed in section 2.5 of Chapter 2, the loading efficiency of ICG affects the absorbance of PIN. In order to get the similar temperature change in PIN, the

absorbance of PIN (2.08 mg/ml) in water was found and matched with different concentration of ICG dissolved in water. It was found that ICG (0.008 mg/ml) showed the similar absorbance (A = 2.5) as compared to 2.08mg/ml PIN (A = 2.62). Also according to the loading efficiency of PIN it was found that 2.1mg/ml of PIN contains 0.01 mg of ICG which is close to the amount of ICG (0.008 mg/ml) used. Hence, similar temperature rise was achieved for ICG and PIN at different concentrations.

A student t-test was performed between control and ICG (0.008, 0.025 and 0.041 mg/ml), as well as control and PIN (2.08, 3.33 and 4.58 mg/ml). Results are shown in figure 3.7 (c) marked by an asterisk (*) for $\alpha < 0.05$. ICG (0.041 and 0.025 mg/ml) and PIN (4.58 mg/ml) showed a significant gain in temperature for all distances compared with the corresponding control phantoms, whereas PIN (2.08 mg/ml) showed significant gain in temperature at 3 mm and 5 mm. In case of ICG (0.008 mg/ml) and PIN (3.33 mg/ml) significant temperature change was found at 3 mm only. Hence, the distance measurements have shown a considerable heat spread till 5 mm in the ICG and PIN with respect to the control.

The temperature profile of control, ICG and PIN phantom measured with respect to time for 3 mm depth from the laser tip is represented in Figure 3.8 (a, b). Similar to the distance measurement, the depth data shows the exponential temperature rise; at the beginning a sharp increase in temperature was found within 60 seconds which gradually increased with time. As observed, control phantom shows a small change in temperature (~2°C) after laser irradiation whereas PIN and ICG phantom have shown a large change

(~8-10 °C). Moreover, ICG and PIN shows identical temperature profile as discussed previously which signifies that PIN has similar heating capability as ICG at different depth also.

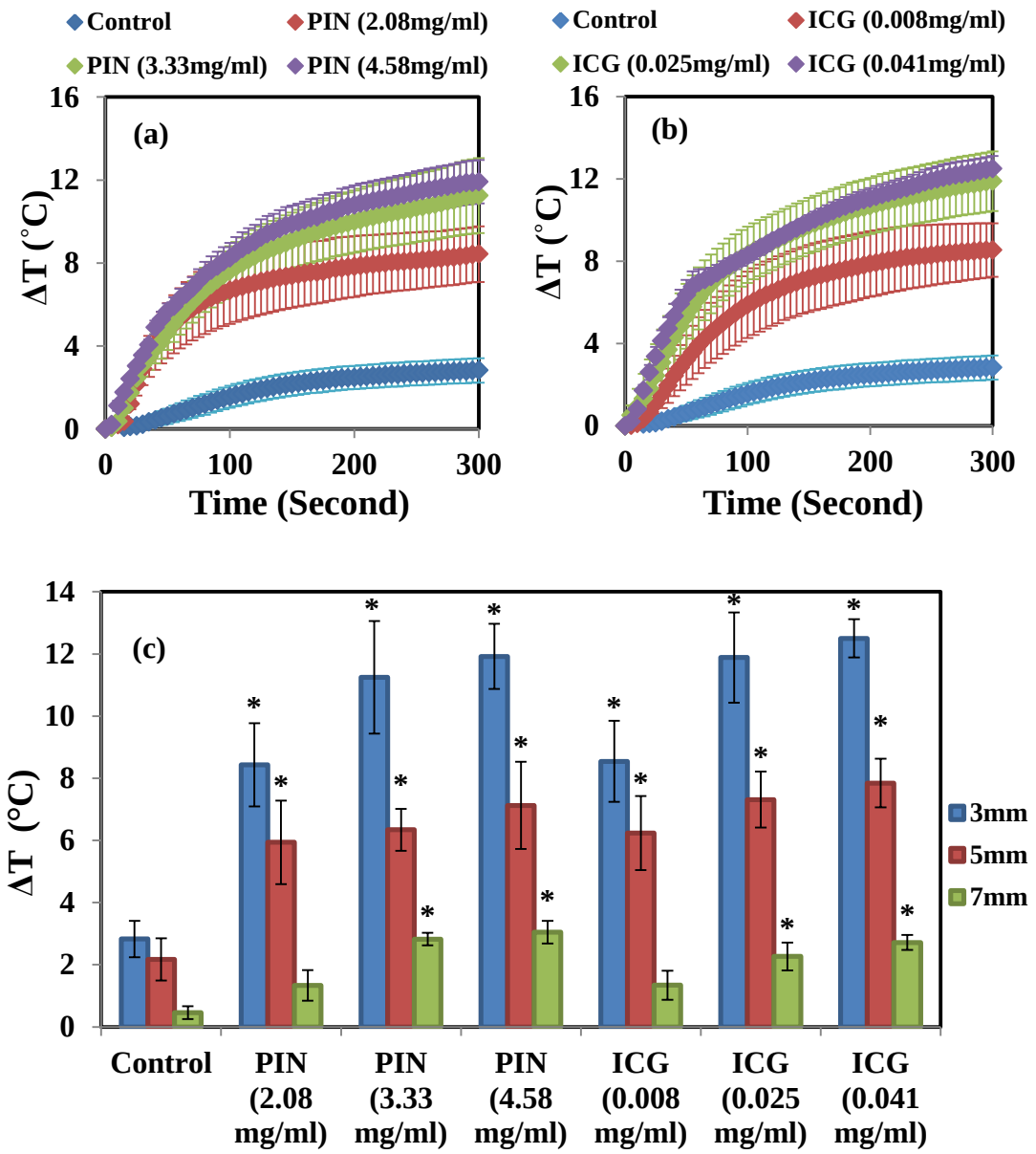

Figure 3.8: Temperature profile with respect to time at 3 mm depth from top surface for (a) PIN and (b) ICG, (c) Peak change in temperature at 3, 5 and 7 mm depth from top surface for Control, PIN and ICG phantoms

Furthermore, Figure 3.8 (c) shows the final temperature achieved after irradiating the phantom for 5 minutes for all the phantoms at 3 mm, 5 mm and 7 mm depth. A gradual decrease in temperature was observed with increasing the depth from 3 mm to 7 mm for all phantoms. It also signifies uniform distribution of heat at shallower depths in the phantom which gradually decreases at larger depths. As seen in Figure 3.8 (c) the temperature change for ICG and PIN phantoms was ~3 times higher than that of control phantom. Also temperature rise was in proportion to the concentration of ICG and PIN . At 3 mm depth, peak ΔT achieved for ICG (0.041, 0.025 and 0.008 mg/ml) was 12.5 ± 0.6, 11.8 ± 1.5˚C and 8.5 ± 1.3˚C respectively whereas for PIN (4.58, 3.33 and 2.08 mg/ml) the same was 11.91 ± 1.0˚C, 11.25 ± 1.8˚C and 8.4 ± 1.2˚C which is sufficient to induce local hyperthermia (42).

A student t-test was performed between control and ICG as well as control and PIN. Significant results are shown in figure 3.8(c) marked by an asterisk (*) for $\alpha < 0.05$. ICG (0.041 mg/ml and 0.025mg/ml) and PIN(4.58 mg/ml and 3.33 mg/ml) showed a significant gain in temperature for all distances compared with the corresponding control phantoms, whereas PIN (2.08 mg/ml) and ICG (0.008 mg/ml) showed significant gain in temperature at 3 mm and 5 mm. Hence, the depth measurements have shown a considerable heat spread till 5 mm in the ICG and PIN with respect to the control phantom. Also, peak temperature achieved for depth measurements were higher than distance measurements because the phantom melts due to continuous irradiation of laser over 5 minutes which shorten the distance from top surface of the phantom to the thermocouple needle poked at various depths. Depth

measurements were hence affected by this and gained higher temperature under the effect of laser irradiation.

Overall, the temperature measurements at different distance and depth validate the capability of PIN to deposit heat sufficient enough to create photothermal effect to destroy tumors. Further verification was carried out by chicken breast tissue embedding intralipid gelatin phantoms whose results are discussed in following section.

3.3 Chicken Breast Phantom Study

In this study I used intralipid gelatin phantom embedded in a chicken breast to quantify PIN and ICG for thermal ablation application. Chicken breast serves an ideal phantom matching animal tissue optical properties (42, 51). A control phantom mimics the simulating tissue model with tumor whereas the ICG and PIN phantoms embedded in chicken breast mimic the tumor tissue targeted with exogenous chromophore. In this study the temperature profile of all the three types of phantoms embedded in chicken breast were examined at different depths and distances.

3.3.1 Experimental Setup

I used the similar experimental setup to the one shown in figure 3.6, only the intralipid gelatin phantom was replaced by a chicken breast phantom. A fresh boneless chicken breast was bought and stored at 3˚C. Before experiment, it was submerge into lukewarm water to bring its temperature back to room temperature. Using a surgical

blade the chicken breast sample was then cut into square piece of 5 x 5 cm and a thickness of 4 cm. A 3 mm thick layer of tissue was cut from the upper surface of the prepared cube. A 3 mm deep hole was made in the center of the sample below the 3 mm flap. Small cylindrical intralipid gelatin phantoms which were previously made were embedded in the chicken breast sample in the hole such that when the flap is closed, the gelatin phantom remains at 3 mm depth from the surface of the sample (Figure 3.9 a). Thermocouples were then inserted in the similar pattern as discussed in Section 3.5.1. The experimental setup for chicken breast phantom study is presented in Figure 3.9 b.

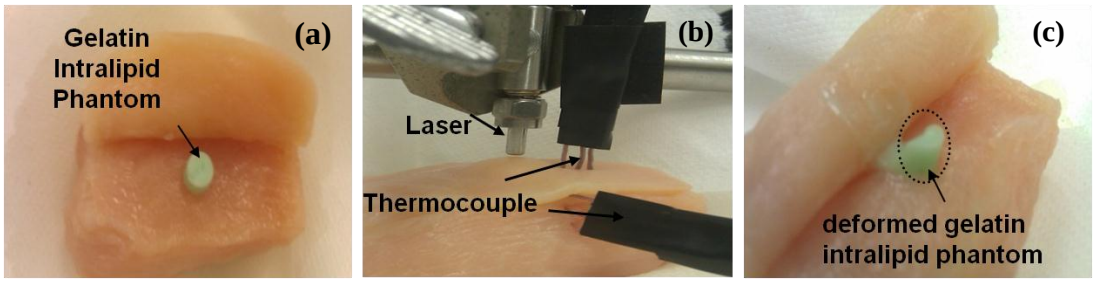

Figure 3.9: (a) Placement of gelatin intralipid phantom within chicken breast tissue (b) Experimental setup and (c) deformed gelatin intralipid phantom after 5 minutes of laser irradiation

3.3.2 Data Acquisition

The chicken breast phantom setup was arranged as shown in figure 3.10 b. The laser, data logger and PC were first turned ON for the experiment. The data was acquired in the similar procedure as described in section 3.5.1. Only the laser current was set at 9 A to achieve the laser irradiation power of 1.55 W for higher penetration. The data were further analyzed and the results will be discussed in the next section.

3.3.3 Results and Discussion

The temperature measurements were taken from chicken breast tissue at 3 mm, 5 mm and 7 mm depths as well as distances from laser tip. Similar data acquisition procedure was carried out as employed in the gelatin phantom study. The temperature difference (ΔT) obtained after 5 minutes of laser irradiation for control, ICG and PIN phantoms are shown in Figure 3.10.

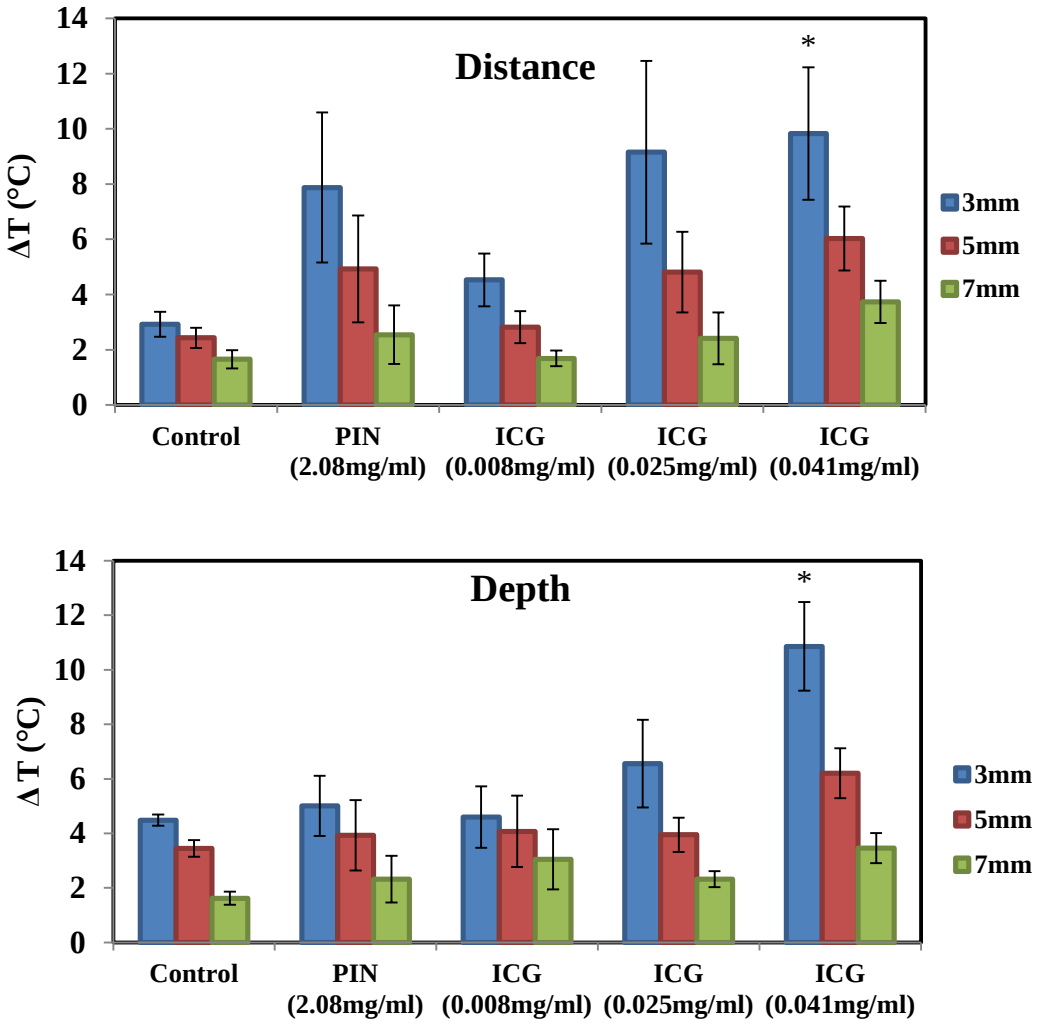

Figure 3.10: Peak temperature changes in Control, PIN and ICG phantoms after 5 minutes of laser irradiation at different (a) Distances and (b) Depth

Figure 3.10 shows the peak ΔT in the chicken breast tissue as a result of laser irradiation for 5 minutes. As seen for gelatin phantoms; the temperature profile was similar for the chicken breast tissue also. At the beginning of laser irradiation there was a steep rise in temperature for 45 seconds which slowed down thereafter and finally reached a constant value. The temperature measured at 3, 5 and 7 mm distances and depth revealed the heat distribution in the chicken breast tissue due to the heating of the gelatin phantoms embedded in it. As seen in Figure 3.10 the temperature rise is considerably higher for ICG (0.041 mg/ml) and ICG (0.025 mg/ml). However, in case of PIN (2.08 mg/ml) and ICG (0.008 mg/ml) I could not gain significant ΔT as compared to control. The intralipid gelatin phantom was embedded inside the chicken breast at 3 mm depth which was heated because of the heat spread through the chicken breast tissue irradiated by the laser. Boundary between the phantom and chicken tissue was not air tight which resulted in lower ΔT compared to that of the previous study in which the laser was directly irradiating the intralipid gelatin phantom. Thus there was no significant rise in temperature was observed for PIN and ICG (0.008 and 0.025 mg/ml) with respect to the control phantom. Although ICG (0.041 mg/ml) had shown a temperature rise of 9.68 ± 1.2˚C and 10.8 ± 0.8˚C for distance as well as depth measurements which were appropriate to induce local heating for hyperthermia treatments (42,51).

A student T- Test was performed between control and ICG (0.008 mg/ml), Control and ICG (0.025 mg/ml), Control and ICG (0.041 mg/ml) as well as control and

PIN. Significant results are shown in figure 3.10(a,b) marked by an asterisk (*) for $\alpha < 0.05$. ICG (0.041 mg/ml) showed a significant gain in temperature for 3 mm depth and distance measurement compared with the corresponding control. Hence, significant temperature difference can be achieved at higher PIN as well as ICG concentration. Moreover, more heating effect can be induced by increasing the laser power.

In summary, for controls maximum gain in temperature achieved was ~2˚C from all depths and distances measurements which is insufficient to cause tumor apoptosis whereas for PIN and ICG phantoms more than 6˚C temperature gain was achieved up to 5 mm depth which can create local heating and can kill cancer cells or destroy the blood vessels (51). Hence, the initial studies have shown promising results for employing PIN for photothermal therapy to treat prostate cancer.

CHAPTER 4

DIAGNOSTIC APPLICATION OF PIN AS A FLUORESCENCE CONTRAST AGENT

4.1 Background

Recently, non invasive mapping of malignancies in tisssue using fluorescence biomarker has gained a significant attention due to the potential of transferring this technology to imaging in animals (19,21,29). In fact, fluorescence imaging has become more feasible due to the available fluorescence probe in NIR range which offers a significant penetration depth in tissue and also the availibility of highly sensitive deteectors such as CCD and ICCD and monochromatic light sources such as white light sources and lasers (21). Though fluorescence imaging allow a better sensitivity and reliable quantitation; it is still difficult to separate the autofluorescence from the body tissue from the fluorescence signal of the probe. However, a multi spectral imaging is a suitable approach that allows to separate the autofluorscence signal from the fluorescence probe and it has shown an excellent sensitivity that is 300 times the conventional fluorescence imaging systems (53).

ICG being a NIR fluorescent dye is widely in use for imaging purpose for tumor diagnosis. ICG encapsulated mesocapsules, mettalic nanoparticles as well as miscelles conjugated with targeting molecule have shown the ability of targeted optical

diagnosis (19,21,29). In chapter 2 optical properties of PIN and ICG were accessed which confirmed the stability of PIN for fluorescence imaging; in addition the conjugation of PIN with R11 peptide that specifically targets prostate cancer, had shown successful cellular uptake.

In this study, I employed a multi spectral imaging system to test the feasibility of R11conjugated PIN for targetting and imaging prostate cancer through *in vivo* experiments.

4.1.1 Instrumentation

Maestro-a multi spectral imaging system (PerkinElmer Inc., Waltham, MA) was employed for the *ex vivo* and *in vivo* studies. The system consists of an imaging chamber with heated stage, liquid crystal tunable emission filters (LCTF), a cooled 16 bit CCD, a 300 Watt xenon based excitation light source (spectral range: 500-950 nm) with interference excitation filters and an anaesthesia manifold as shown in figure 4.1.

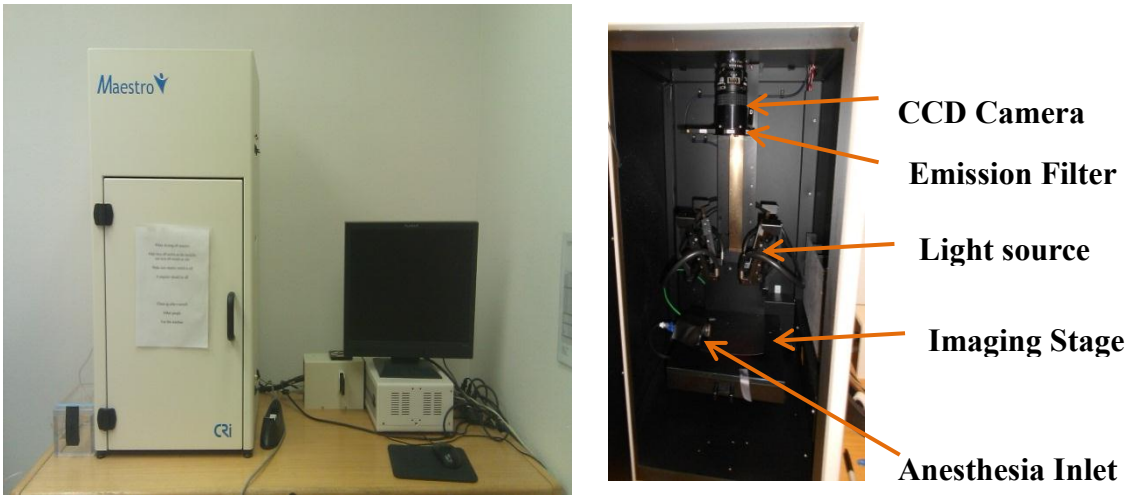

Figure 4.1: Image of the Maestro imaging system

Excitation light is delivered to the imaging chamber via four fiber-optic adjustable illuminator arms which yield an even distribution to the subject from the top. The light radiating from the excitation source and filter passes through the sample to the long pass emission. The light then passes through the camera lens and through the LCTF and finally to the CCD. LCTF allows fast, accurate wavelength change with a narrow bandwidth of 2 nm (53,54). They use polarization in their spectral selection process hence, their transmission efficiency is low (~30%) compared to traditional interference filters (~90%). However, Spectral information gained while performing multi spectral imaging outweighs the impact of lower transmission efficiency (54). Anesthesia unit of imager has one inlet connected to the nose cone to keep the animal under mild anesthesia during measurements and another connected to the induction chamber to anesthetize the animal prior imaging. Isofluorene is used as an anesthetic agent for this system. Isofluorene is mixed with oxygen within the anesthesia unit. Isofluorene concentration is also set by the vaporizer control knob that can be monitored from the isofluorene glass slit. The gas flow control knob controls the flow of oxygen from O_2 tank is checked by the flow meter.

4.1.2 Working Principle

The working principle of multi-spectral imaging is shown in Figure 4.2. The liquid crystal tunable filter allows the camera to capture images at different wavelengths for a user defined wavelength range that forms a RGB image with each pixel

representing a spectral component of the scanned wavelength. It is difficult to identify the fluorophore of different emission wavelengths from the RGB image.

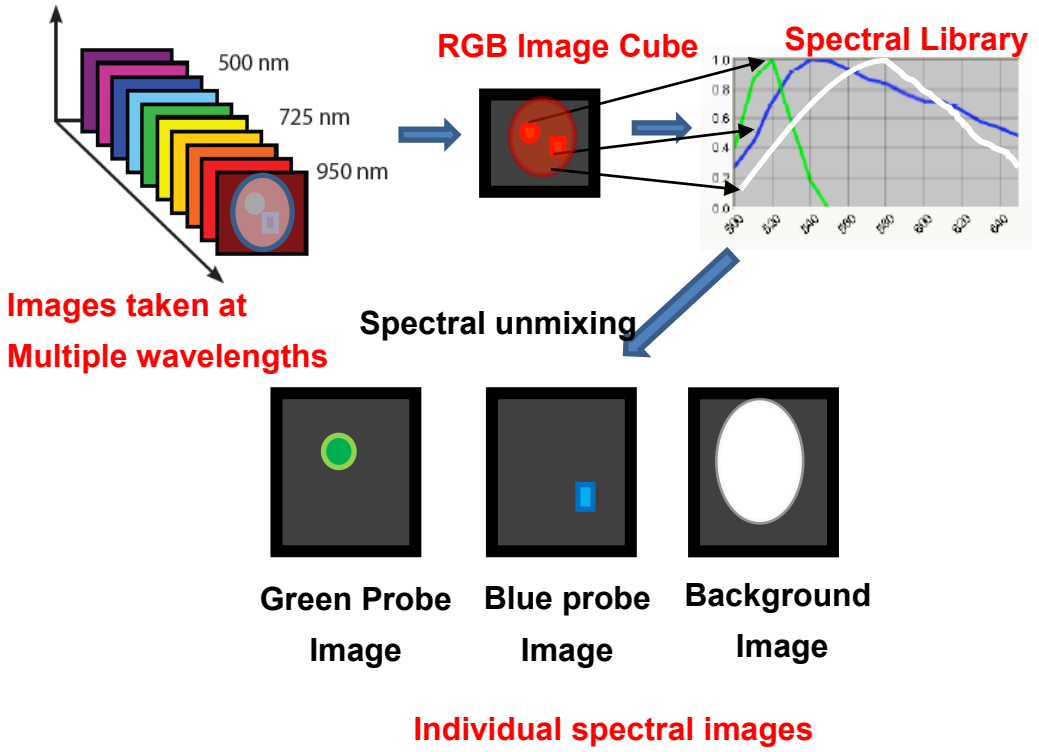

Figure 4.2: Illustration of steps to build spectral library and unmixing the pure spectra

The spectral unmixing allows to separate the spectral component of fluorescent probe at different wavelength from the background (53). Spectral unmixing is nothing but a spectral classification algorithm (55). It assumes each pixel is made up of combination of pure spectra.

$$Sxy = Lw$$

Where, Sxy is a vector containing the spectrum at a pixel and L is a matrix with n pure spectra and m spectral channels. Algorithm solves the equation for w, which

represents the contribution of each pure spectrum in L to a pixel Sxy in the image. Finally, from least square approximation it finds the best w (55).

$$e = ||\mathrm{Lw} - \mathrm{Sxy}||^2$$

Thus, the final image porcessing provides images of the fluorescent probes separated from the background as well as the composite image of the fluorescent probe with the background signal. This principal aids in increasing the signal to noise ratio of the fluorescence signal of the probe.

4.1.3 Software

Maestro Software is the image acquisition and analysis product from PerkinElmer Inc. The fundamental advantage of the Maestro fluorescence imager and software is its ability to reduce signal-to-noise ratio 300-fold by the process of separating individual fluorophores from each other and from background autofluorescence. Its resolution is capable of unmixing a large range of multi-spectral fluorophores that may overlap and to extract their pure signals. Because the Maestro scans images between 500 and 950 nm, this range reduces the problem correlated with tissue absorption. In addition, selecting for autofluorescence/background within any wavelength range has the potential to eliminate all background signals. Therefore, the function of selecting and filtering this obtrusive signal yields a pure form of the signal of interest. It provides easy to use control panels that set and display all imaging parameters, from exposure time to wavelength ranges. Once acquisition is complete, the

analysis section can quickly and accurately extract the desired fluorescent signal from autofluorescence background (54).

4.2 *Ex vivo* Tissue Imaging

Ex vivo tissue imaging was performed in chicken breast tissue phantom with PIN and ICG solution filled capillaries placed on surface as well as at various depths in the tissue phantom. The fluorescence signals from the phantoms embedding ICG and PIN capillaries at various depths were measured in order to examine the deep tissue imaging capacity of PIN as well as ICG.

4.2.1 Sample Preparation

Fresh chicken breast tissue was purchased one hour before imaging and stored at room temperature. PIN as well as ICG were dissolved in PBS to make a final concentration of 10 mg/ml and 20 mg/ml for PIN whereas 50 µg/ml and 100 µg/ml for ICG. From the prepared solutions 50 µl of suspension was filled in a capillary open at both the ends. The capillaries were then sealed with paraffin wax paper to prevent leakage of the solution. The glass capillaries filled with ICG and PIN were covered with an aluminum foil and stored at room temperature.

4.2.2 Data Acquisition

The CRi Maestro imaging system described above was employed for phantom imaging.A bandpass excitation filter (690- 700 nm) and 750 nm long-pass LCTF

emission filters were placed in their respective location. The light source and the imaging system were turned ON. A chicken breast tissue cut into 3 x 7 x 7 cm^3 cube was placed on the imaging table in the imaging chamber. The system door was locked for acquiring the image. The maestro software was used for image acquisition. In the acquire tab the image exposure time was set at 5000 ms and the images were acquired between 700 – 950 nm with a step size of 10 nm which resulted in an image cube of 26 images.

Initially, image cube of the prepared tissue phantom was captured and stored as a background image cube. This data was later used for background subtraction. Then, the capillary filled with PIN was placed on the surface of the same tissue phantom and the image cube was again acquired. Thereafter, the tissue sample was cut 3 mm below the top surface parallel to horizontal axis to create an opening to place the ICG/PIN filled capillary and data was acquired. Similarly the images were acquired for the capillary located at 5, 7 and 11 mm for all concentrations of ICG as well as PIN. The acquired image cube for all the measurements was further processed and the change in fluorescence signal as a function of depth was analyzed which is discussed in the next section.

4.2.3 Results and Discussion

The previously acquired images were further analyzed by spectrally unmixing the background (autofluorescence) spectra of the tissue from the fluorescence spectra of ICG or PIN. A true image of the fluorescent probe without any autofluorescence was thus obtained. A specific ROI from the true image was selected and the total photon

counts were obtained. The fluorescent intensity measured from PIN and ICG capillaries is plotted as a function of depth as shown in figure 4.4.

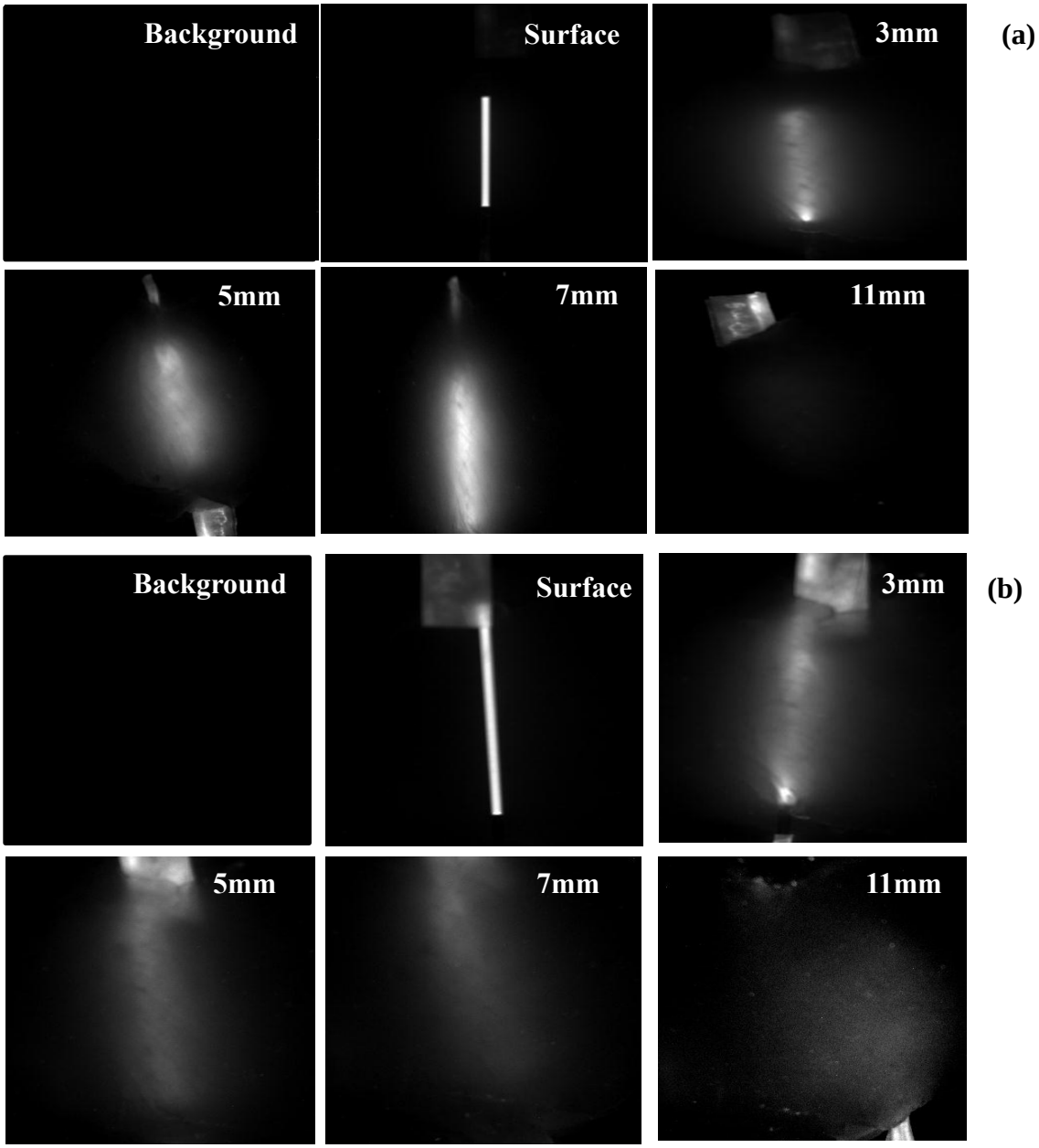

Figure 4.3: Fluorescence intensity Images of (a) 10 mg/ml PIN (b) 100µg ICG filled capillaries placed on surface, 3 mm, 5 mm, 7 mm and 11 mm depth of chicken breast tissue

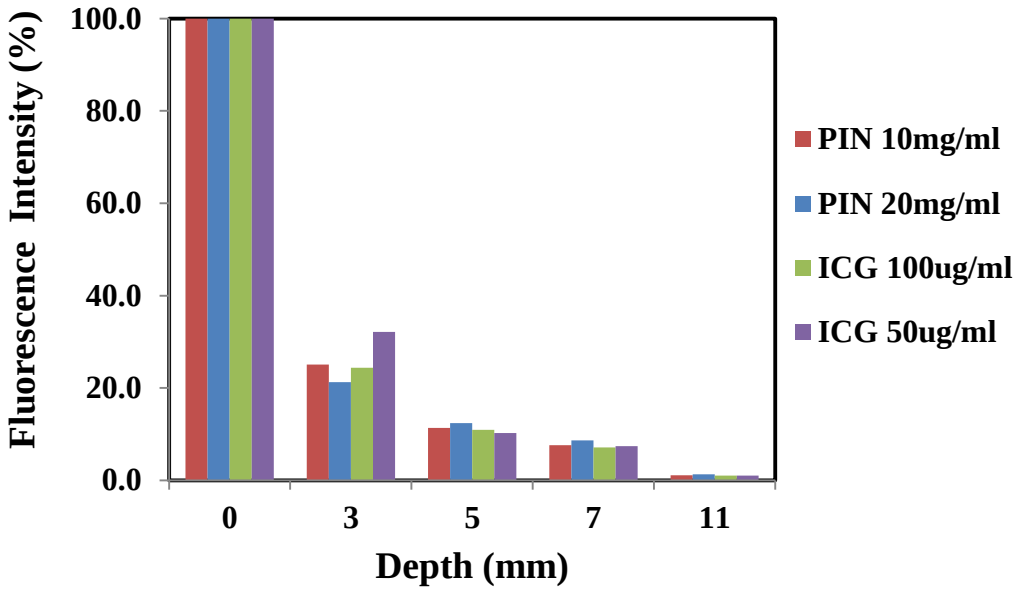

Figure 4.4: Fluorescence intensity measurements of PIN and ICG for different concentration and at various depths

Figure 4.3 shows the fluorescence images of PIN and ICG filled capillaries acquired at different depths in a chicken breast tissue. The background image of the tissue sample was captured to obtain the autofluorescence signal. Further, the images of the capillary placed on surface as well as different depth in the tissue shown in figure were obtained by subtracting the tissue autofluorescence through spectral unmixing. It was observed that capillary placed on surface shows clear edges whereas the capillary becomes diffused because of light scattering in tissue. Figure 4.4 shows the fluorescent intensity counts obtained at different depths for ICG and PIN. Considering the intensity counts obtained on surface as 100% counts, relative intensity counts from further depths were calculated. It was observed that at 3 mm depth, a sharp decrease in intensity by 70 – 80% for ICG as well as PIN was seen due to light scattering and absorption due to surrounding tissue. The intensity gradually decreased at further depths and at the depth

of 11 mm almost 99% decrease in fluorescence intensity was seen as compared to the surface measurements.

Hence, the results of tissue fluorescence imaging till 11 mm depths highlights the optically transparent nature of PIN and ICG in highly scattering tissue imaging applications. The property of PIN and ICG to strongly absorb light and emit fluorescence in NIR range makes it suitable for non-invasive deep tissue imaging. Thus, this study demonstrates the capability of PIN for *in vivo* tumor imaging.

4.3 *In vivo* Animal Imaging

All animal experiments were performed according to approved ptotocol of Institutional Animal Care and Use Committee. A whole body animal imaging was performed on mice to investigate the *in vivo* distribution of R11 conjugated PIN and non-conjugated PIN. NIR fluorescence imaging measurements will reveal the capacity of PIN for targeting and non-invasive diagnosis of prostate cancer. The experiment contained four different animals groups as shown below:

Table 4.1: Four different animal groups used for the in vivo imaging

Control Group	Injecting non Conjugated PIN
	Injecting R11 peptide Conjugated PIN
Tumor Group	Injecting non Conjugated PIN
	Injecting R11 peptide Conjugated PIN

Fluorescence signals were compared for four animal groups; the control group and the tumor group targeted with R11 conjugated and non-conjugated PIN.

4.3.1 Animal Preparation

20 SCID – NOD mice of 6 – 8 week were used for the study. Ten mice were used as control group without tumors. The other ten mice were used for the tumor group and tumor was grown on the two sites on the back via subcutaneous injection. The mice under tumor group were injected with 1x 10^6 PC3—KD prostate cancer cells per site. The tumor was allowed to grow for a week.

4.3.2 Experimental procedure

Prior to the experiment 13.25 mg PIN (21,29) were conjugated with 1 µM R11 peptide in 1 ml of PBS using the same conjugation method described previously in chapter 2. Before imaging, the animals were placed in the induction chamber with 2.5% Isofluorane mixed with oxygen for 3 minutes to anesthetize them. Abdomen area was shaved to prevent scattering of light due to fur. Once shaved, they were anesthetized and placed in the imaging chamber one at a time for whole body imaging as shown in Figure 4.5. For the imaging chamber the isofluorene gas flow was kept at 1.5%.

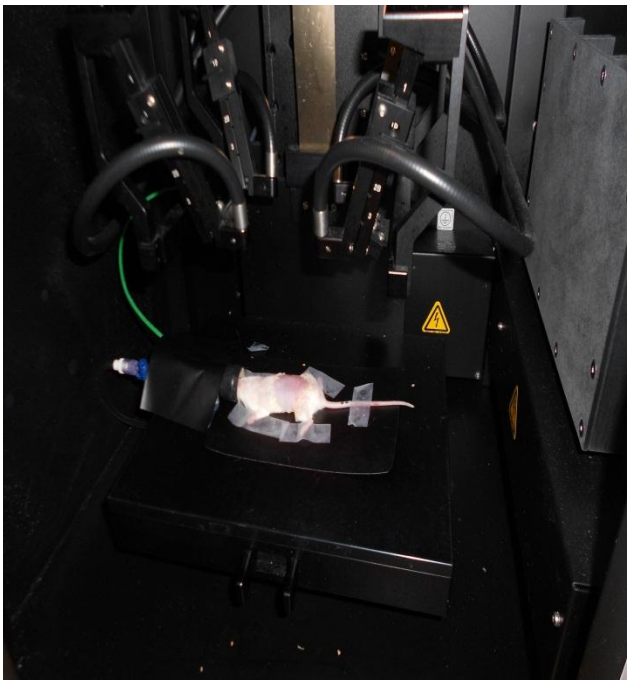

Figure 4.5: Mouse placed in imaging chamber

Images were captured in the spectral range from 700 – 950 nm. The baseline image was thus taken without injecting PIN. Further, after baseline measurement, 100 µl of non-conjugated PIN / R11 conjugated PIN was injected intravenously in the tail of the animals. The animals were imaged at 1, 2, 4 and 6 hours of post injection. The animals were anaesthetized each time prior imaging. After 6 hour time point, animals were euthanized in CO_2 chamber and the liver, kidneys, spleen and the prostate/tumor were dissected and placed on the imaging plate. The organs were imaged using the imaging system with excitation and emission filter settings described in the previous section and the multispectral image cube was acquired.

4.3.3 Data Analysis

The previously acquired images were analyzed using Maestro software. The baseline images were taken before injection. The region of interest (ROI) with high autofluorescence signal was selected using a white color marker and the obtained spectrum was saved in a spectral library. A screen shot of the autofluorescence signal obtained from the mouse with baseline measurements is shown in figure 4.6.

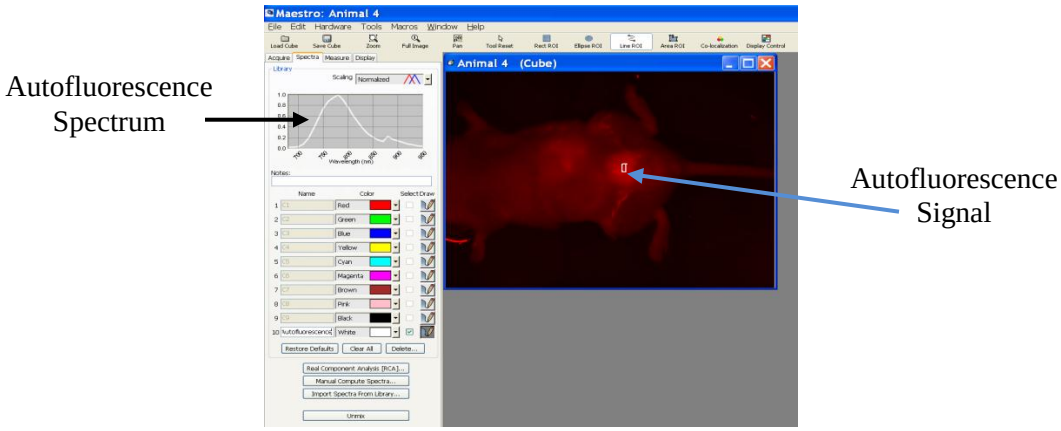

Figure 4.6: Representation of autofluorescence spectrum from baseline mouse

Thereafter, an image at 1 hour post injection from the same animal was opened and PIN + autofluorescence profile was obtained. Pure PIN profile was then obtained through ‘manual compute spectra’ tab. Finally, the ‘unmix’ tab was used which run unmixing algorithm as described in section 4.1.2 to separate the autofluorescence signal from the PIN. The algorithm gave 3 images as output: (1) autofluorescence signal, (2) pure PIN signal and (3) An overlay composite image: fluorescence signal from PIN (green) on autofluorescence background signal (white). Figure 4.7 is an illustrative

screenshot of unmixing steps and outcomes. The composite image was saved for data representation and the two component images were used for intensity calculations.

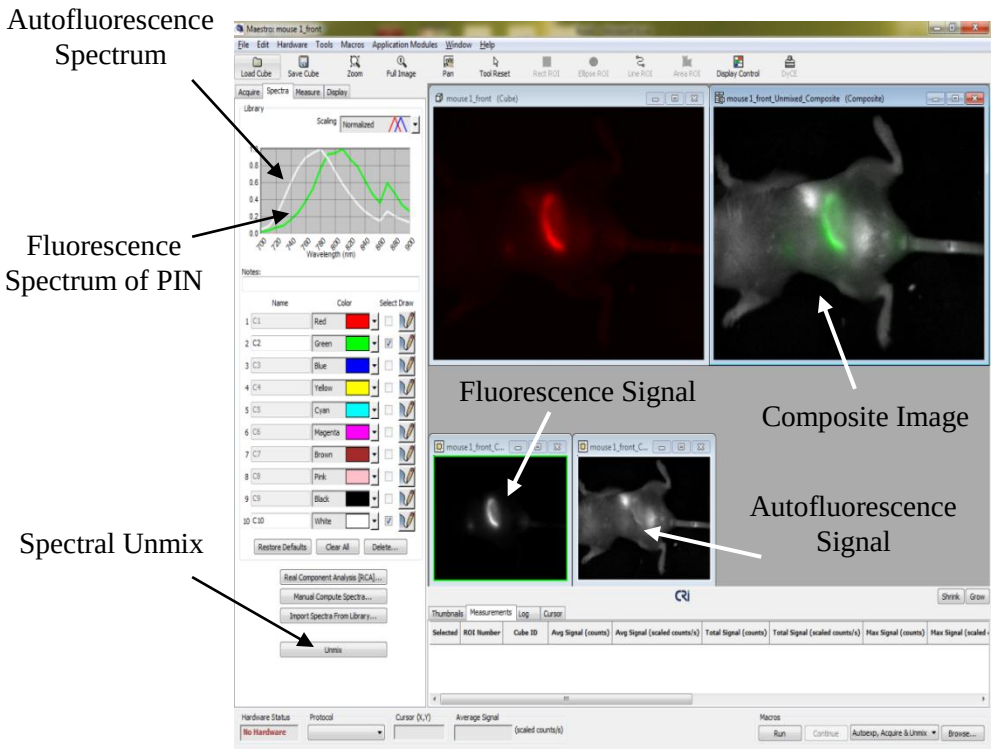

Figure 4.7: Spectral unmixing of image with fluorescne signal

For intensity measurements the ‘Measure’ tab in the software was clicked. The ROI was drawn over the maximum intensity areas and toal signal (Scaled counts/ Sec) was used as a comparative parameter between time points.

4.3.4 Results and Diuscussion

The acquired images at baseline and at different time points were analyzed according to the spectral unmixing process discussed above. The composite image containing the fluorescence from PIN with the interfering autofluorescence from an anesthetized mouse were evaluated for control and tumor group as shown in Figure 4.8 and 4.9

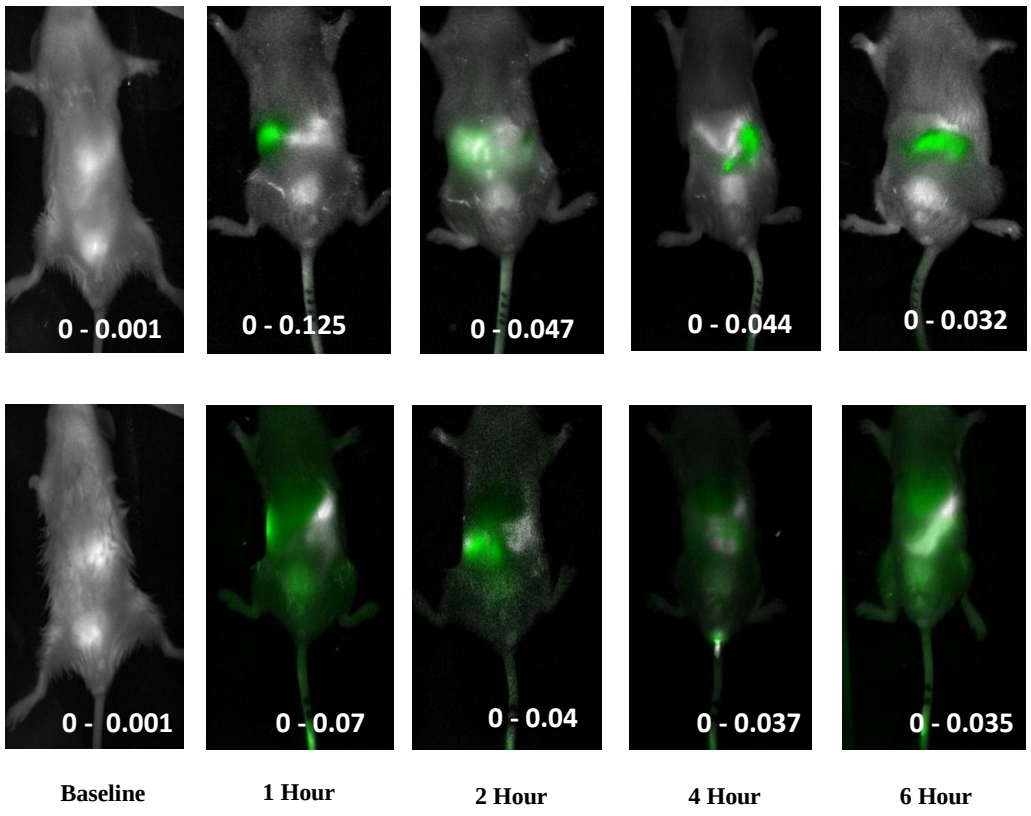

Figure 4.8: *In vivo* imaging for control group for before and after i.v injection of non-conjugated PIN (top) and R11 conjugated PIN (bottom)

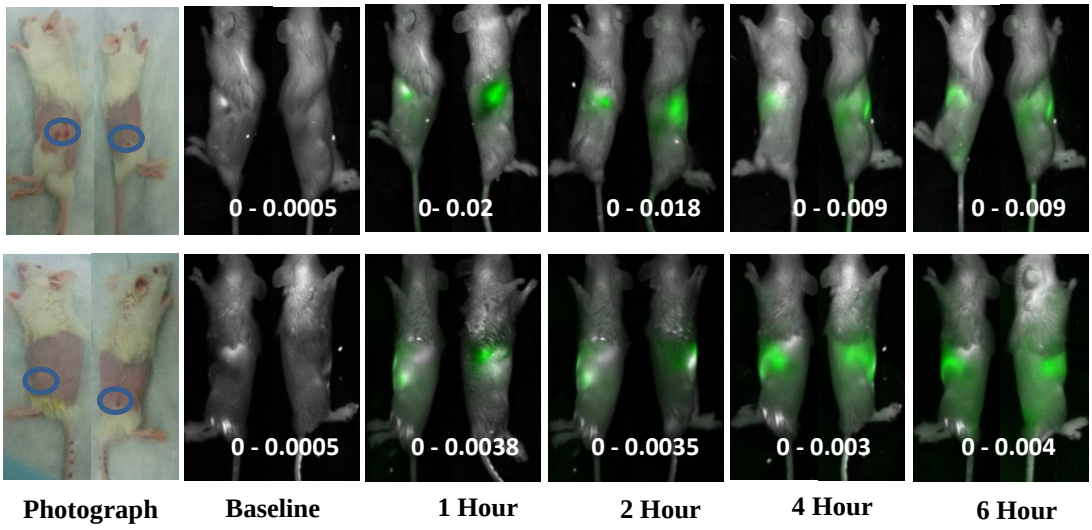

Figure 4.9: *In vivo* tumor imaging for tumor group before and after i.v injection of Non-conjugated PIN (top) and R11 conjugated PIN (bottom)

In figure 4.8 and 4.9 the images represent the distribution of non-conjugated/ R11 conjugated PIN at different time after injection. The numbers represents the maximum and minimum fluorescence intensity value at each time point. The baseline image taken before injection shows weak autofluorescence signal prior to PIN injection. Longest possible exposure time (5000 ms) was used to acquired this weak signal. After the PIN injection, the animal was imaged after 1 hour which showed a strong fluorescence signal (shown by green color) of PIN from the liver for both conjugated and non conjugated PIN. Even after 6 hours post injection the flourescence signal was observed from the liver. (Figure 4.8).

In addition, the tumor group with tumor grown on two sides of foreback as shown in figure 4.9 were also evaluted to monitor the distribution of PIN. The anestehtized mice were placed in dorsoventral position for imaging prior to the PIN administration which showed negligible autofluorescence signals. After 1 hour post injection a strong signal was observed from the liver as seen previously for the control group. Even after 6 hours post injection, conjugated and non-conjugated PIN were remained accumulated in the abdominal area showing a high fluorescence in liver (figure 4.9). Some of the signal was also observed from the tail due to accumulation of PIN in the tail during injection. Findings from in vivo imaging were further validated via biodistribution study of PIN. The liver, kidneys, spleen and prostate / tumors were imaged and the fluorescence intensity were measured to gain insights of PIN biodistribution. Figure 4.10 shows the white light image and the fluorescence image of dissected organs for non-conjugated PIN.

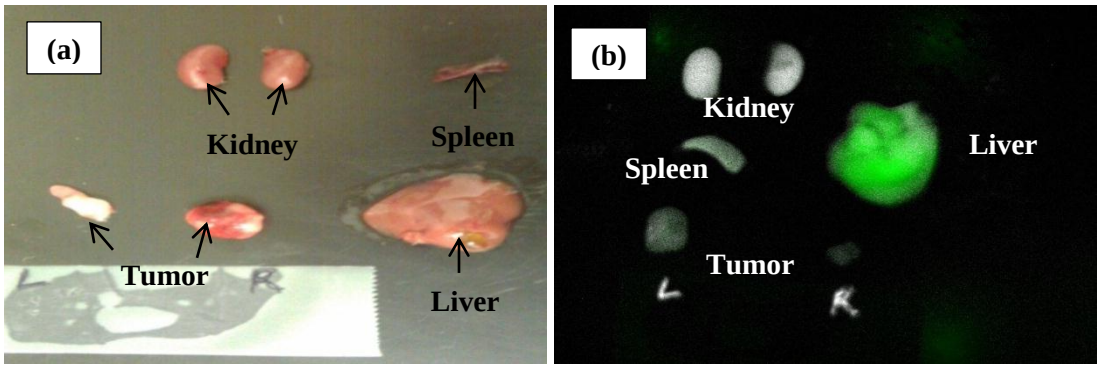

Figure 4.10: Dissected organs from a sacrificed mouse after i.v. injection of non cojugated PIN (a) white light image (b) fluorescent image

In order to quantify the fluorescene intensity, first a ROI was drawn over each organ and total fluorescene intensity (scaled counts/sec) was measured within them.

Thereafter, total intensity was normalized by dividing it with its corresponding ROI area.

$$Normalized\ intensity = \frac{Total\ signal\ withing\ ROI(scaled\frac{count}{sec})}{Area\ of\ ROI\ (mm^2)}$$

The normalized intensity was then used for direct comparison of intensity between different organs. Figure 4.10(b) suggests that the major fluorescence from the visceral organs was contributed by the liver. This finding was further confirmed by plotting the normalized fluorescence intensity from various organs in figure 4.11. Both the groups show high liver uptake of conjugated and non-conjugated PIN. Whereas fluorescent intensity observed in other organs were 50% - 70% less than liver for control group and 80% – 90 % less for tumor group.

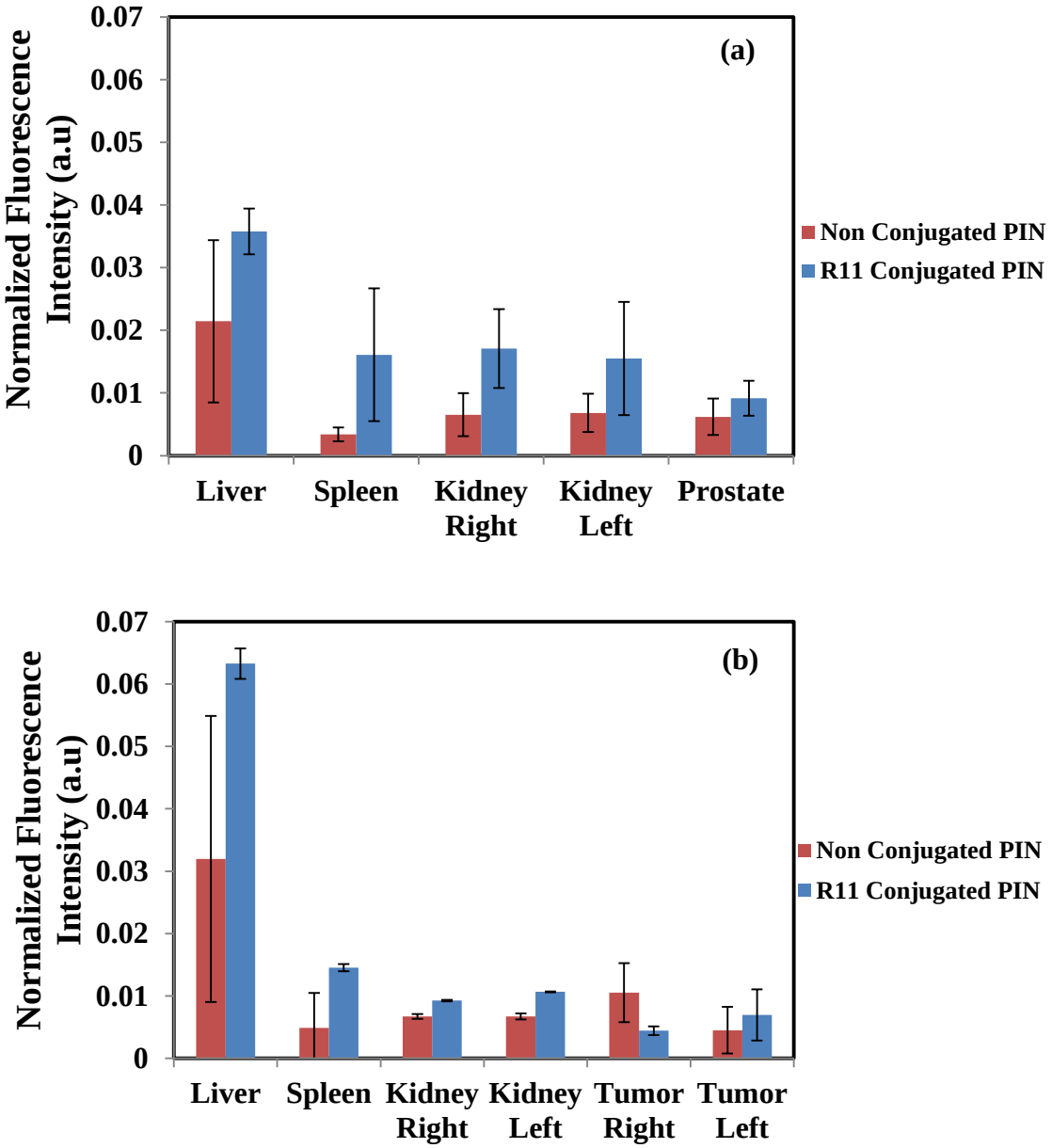

Figure 4.11: Biodistribution of non conjugated/ R11 conjugated PIN in Liver, Spleen, Kidneys and Tumors for (a) Control group and (b) Tumor group

The accumulation of nanoparticles in liver was also observed in previous studies on different type of nanoparticles (21). The efficiency of targetting of PIN to prostate

tumor could be tuned by controlling the particle size and surface charge of PIN. Literature suggets that the ideal particle size for prostate targetting should be in 50 – 100 nm range (21). PIN of large particle size were unable to target tumor because they could not invade the smaller tumor vasculature and got acculmulated in the liver as it funtions to metabolize larger substances.

In summary, PIN have been successful in enhancing optical contrast for *in vivo* whole body imaging. In addition to that the autofluorescence from the tissue is less in the NIR range allowing to image at a great penetration depth. Thus, by fine tunning the fabrication process of PIN to get 50-100 nm partical size can aid in tumor imaging at greater depths for future studies.

CHAPTER 5

CONCLUSION AND FUTURE WORK

5.1 Conclusion

Multifunctional PIN were succesfully synthesized with a mean particle size of 246 nm and 48.5% of ICG entrappment efficiency. The optical characterizaation of PIN in terms of excitation emission spectra, flourescence intensity and absorption spectrum demonstrated its stability as compared with ICG in various biorelevant solvents over extended period of time. It was also observed that PIN plays an important role in preserving the optical porperties of ICG. The fluorescence lifetime of ICG obtained was 0.19 ns whereas for PIN was increased to 0.29 ns due to the PLGA shell in PIN. The cell viability study verified the cytocompatibility of PIN. The cellular uptake study confirmed the high binding efficiency of R11 conjugated PIN with PC3 cells. PIN were successful in obtaining significant temperature gain that is required for hyperthermia treatments through gelatin intralipid and chicken breast phantoms studies. Results suggest the great potential of PIN to induce local hyperthermia for therapeutic interventions by allowing long term stability. In addition, the fluorescence property of PIN was evaluated to enhance fluorescence contrast through *ex vivo* tissue and *in vivo* animal imaging. PIN have proven its ability of image enhancement for deep tissue imaging in ex vivo tissue phantom study.

In summary, PIN have shown the capability for enhance tumor imaging and therapeutic applications with encouraging results.

5.2 Future Work

The potential of PIN as a fluorescent contrast agent has shown promising results. Decreasing the particle size would make them more efficient for targeting which would aid in noninvasive tumor imaging. The therapeutic application of PIN can be further revised through animal studies. The strong absorption of PIN at NIR wavelength makes them suitable for DOT which has shown a great potential in imaging at greater depths. Hence, in future the application of PIN as DOT contrast agent can be studied. Recently, ICG as a PA contrast agent has been studied by various groups. Thus, feasibility of PIN for photoacoustic imaging applications can be evaluated. Multifunctional PIN can be thus applied for various optical imaging modalities.

REFERENCES

1) http://men.webmd.com

2) http://med.myseda.com/anatomy.php/prostate

3) http://www.buzzle.com/articles/prostate-gland-function.html

4) http://www.umm.edu/altmed/articles/prostate-cancer-000028.htm

5) http://www.medicinenet.com/prostate_cancer/article.htm

6) http://www.consumersresearchcncl.org/Healthcare/Oncologists/oncol_chapters_2.html#top

7) G. D. Grossfeld and P. R. Carroll, "Prostate cancer early detection: a clinical perspective," Epidemiol Rev. 23, 173-80 (2001).

8) Francesco Pinto, Angelo Totaro, Alessandro Calarco, Emilio Sacco, Andrea Volpe, Marco Racioppi, Alessandro D'Addessi, Gaetano Gulino, PierFrancescoBassi. "Imaging in Prostate Cancer Diagnosis: Present Role and Future Perspectives" UrolInt 2011;86:373–382

9) Hassan FU, Mohan HK, Gnanasegaran G, Vijayanathan S, Fogelman I. "Beware

of the focal uptake at the ischium on the bone scan in prostate cancer".Nucl Med Commun. 2011 Apr;32(4):320-3

10) Seo Y, Aparici CM, Chen CP, Hsu C, Kased N, Schreck C, Costouros N, Hawkins R, Shinohara K, Roach Iii M." Mapping of lymphatic drainage from the prostate using filtered 99mTc-sulfur nanocolloid and SPECT/CT."J Nucl Med. 2011 Jul;52(7):1068-72. Epub 2011 Jun 16

11) http://www.nextgenerationpdt.com/pages/view/information_question

12) Sylvain Gioux, HakSoo Choi, and John V. Frangioni. "Image-Guided Surgery using Invisible Near-Infrared Light:Fundamentals of Clinical Translation" Mol Imaging. 2010 October ; 9(5): 237–255.

13) Jibe Yu, David Javier, Mohammad A. Yaseen, Nit in Nit in, Rebecca Richards-Kortum, Brahman Anvari, and Michael S. Wong, "Self-assembly synthesis, tumor cell targeting, and photo thermal capabilities of antibody-coated indocyanine green nanocapsules" J Am Chem Soc. 2010 February 17; 132(6): 1929-1938.

14) Kim TH, Chen Y, Mount CW, Gombotz WR, Li X, Pun SH "Evaluation of temperature-sensitive, indocyanine green-encapsulating micelles for noninvasive near-infrared tumor imaging."PHARMACEUTICAL RESEARCHVolume 27, Number 9, 1900-1913

15) A.H. Hielscher, A.Y. Bluestone, G.S. Abdoulaev, A.D. Klose, J. Lasker, M. Stewart, Netz and J. Beuthan," Near-infrared diffuse optical tomography", Disease Markers 18 (2002) 313–337.

16) Shan Jiang, Muthu Kumara Gnanasammandhan and Yong Zhang "Optical imaging-guided cancer therapy with fluorescent nanoparticles" J. R. Soc. Interface published online 16 September 2009

17) Lilian E van Vlerken & Mansoor M Amiji "Multi-functional polymeric nanoparticles for tumour-targeted drug delivery" Expert Opin. Drug Deliv. (2006) 3(2):205-216

18) Vishal Saxena, MostafaSadoqi, Jun Shao. "Indocyanine green-loaded biodegradable nanoparticles: preparation, physicochemical characterization and in vitro release" International Journal of Pharmaceutics 278 (2004) 293–301

19) Tae Hee Kim, Yongping Chen, Christopher W Mount, Wayne R Gombotz, Xingde Li, Suzie H Pun. "Evaluation of temperature-sensitive, indocyanine green-encapsulating micelles for noninvasive near-infrared tumor imaging." Pharmaceutical Research (2010) Volume: 27, Issue: 9, Pages: 1900-1913

20) Altinoğlu EI, Russin TJ, Kaiser JM, Barth BM, Eklund PC, Kester M, Adair JH. "Near-infrared emitting fluorophore-doped calcium phosphate nanoparticles for in vivo imaging of human breast cancer." ACS Nano. 2008 Oct 28;2(10):2075-84.

21) Chia-Hung Lee, Shih-Hsun Cheng, Yu-Jing Wang, Yu-Ching Chen,Nai-Tzu Chen, Jeffrey Souris, Chin-Tu Chen, Chung-Yuan Mou, Chung-Shi Yang, Leu-Wei Lo. "Near-Infrared Mesoporous Silica Nanoparticles for Optical Imaging: Characterization and In vivo Biodistribution" Advanced Functional Materials Volume 19, Issue 2, pages 215–222, January 23, 2009

22) Kocbek P, Obermajer N, Cegnar M, Kos J, Kristl J. "Targeting cancer cells using PLGA nanoparticles surface modified with monoclonal antibody." J Control Release. 2007 Jul 16;120(1-2):18-26. Epub 2007 Mar 30

23) Kohl Y, Kaiser C, Bost W, Stracke F, Thielecke H, Wischke C, Lendlein A, Kratz K, Lemor R. "Near-infrared dye-loaded PLGA nanoparticles prepared by spray drying for photoacoustic applications." Int J Artif Organs. 2011 Feb;34(2):249-52.

24) Xu JS, Huang J, Qin R, Hinkle GH, Povoski SP, Martin EW, Xu RX "Synthesizing and binding dual-mode poly (lactic-co-glycolic acid) (PLGA) nanobubbles for cancer targeting and imaging" Biomaterials. 2010 Mar; 31(7):1716-22. Epub 2009 Dec 16.

25) Xu RX, Huang J, Xu JS, Sun D, Hinkle GH, Martin EW, Povoski SP "Fabrication of indocyanine green encapsulated biodegradable microbubbles for structural and functional imaging of cancer." J Biomed Opt. 2009 May-Jun;14(3):034020

26) Gomes AJ, Lunardi LO, Marchetti JM, Lunardi CN, Tedesco AC "Indocyanine green nanoparticles useful for photomedicine." Photomed Laser Surg. 2006 Aug;24(4):514-21.

27) Vishal Saxena, Mostafa Sadoqi, Jun Shao , "Enhanced photo-stability, thermal-stability and aqueous-stability of indocyanine green in polymeric nanoparticulate systems" Journal of Photochemistry and Photobiology B: BiologyVolume 74, Issue 1, 19 March 2004, Pages 29-38

28) Yasuhiko Iwasaki, Shin-ichi Sawada, Kazuhiko Ishihara, Gilson Khang, Hai Bang Lee **"**Reduction of surface-induced inflammatory reaction on PLGA/MPC polymer blend" BiomaterialsVolume 23, Issue 18, September 2002, Pages 3897-3903

29) XiaohuiZheng, Da Xing, Feifan Zhou, Baoyan Wu, and Wei R. Chen "Indocyanine Green-Containing Nanostructure as Near Infrared Dual-Functional Targeting Probes for Optical Imaging and Photothermal Therapy" *Mol. Pharmaceutics*, 2011, 8 (2), pp 447–456

30) Yuan Tang, Anthony J. McGoron "Combined effects of laser-ICG photothermotherapy and doxorubicin chemotherapy on ovarian cancer cells"Journal of Photochemistry and Photobiology B: BiologyVolume 97, Issue 3, 2 December 2009, Pages 138-144

31) Tae Hee Kim, Yongping Chen, Christopher W Mount, Wayne R Gombotz, Xingde Li, Suzie H Pun "Evaluation of temperature-sensitive, indocyanine green-encapsulating micelles for noninvasive near-infrared tumor

imaging.”Pharmaceutical Research (2010)Volume: 27, Issue: 9, Pages: 1900-1913

32) Yvonne Kohl, Dipl-Food Chem, Christian Kaiser, Drrernat, Wolfgang Bost, Dipl-Phys, Frank Stracke, Drrernat, Marc Fournelle, Dipl-Phys, Christian Wischke, Drscnat , Hagen Thielecke, Dr-Ing, Andreas Lendlein, Drscnat, Karl Kratz, Drrernat, Robert Lemor, Drrerna “Preparation and biological evaluation of multifunctional PLGA-nanoparticles designed for photoacoustic imaging” Nanomedicine: Nanotechnology, Biology and Medicine Volume 7, Issue 2, April -2011, 228 - 237

33) Avnesh Kumari, Sudesh Kumar Yadav, Subhash C. Yadav “Biodegradable polymeric nanoparticles based drug delivery systems” Colloids and Surfaces B: Biointerfaces, Volume 75, Issue 1, 1 January 2010, Pages 1-18

34) JayanthPanyam, VinodLabhasetwa “ Biodegradable nanoparticles for drug and gene delivery to cells and tissues. “ Advanced Drug Delivery Reviews, Volume 55, Issue 3, 24 February 2003, Pages 329-347.

35) Yuan Tang, Tinguin Lei, RomilaManchanda, AbhignyanNAgesetti, Alicia Fernandez, SupriyaSrinivasan, Anthony J. McGoron. “ Simultaneous delivery of Chemotherapeutic and Thermal Optical Agents to Cancer Cells by a Polymeric (PLGA) Nanocarrier: An In Vitro Study” Pharm Res(2010) 27: 2242-2253

36) Anna Gerega, Norbert Zolek, Tomasz Soltysinski, Daniel Milej, PiotrSawosz, BeataToczylowska, and Adam Liebert “Wavelength-resolved measurements of

fluorescence lifetime of indocyanine green" Journal of Biomedical Optics 16(6), 067010 (June 2011)

37) Mikhail Y. Berezin1, Hyeran Lee1, Walter Akers1, Kevin Guo1, Reece J. Goiffon1, Adah Almutairi2, Jean M. J. Fréchet3, Samuel Achilefu1,4. "Engineering NIR Dyes for Fluorescent Lifetime Contrast" 31st Annual International Conference of the IEEE EMBS Minneapolis, Minnesota, USA, September 2-6, 2009

38) Sylvain Gioux1,2, HakSoo Choi1, and John V. Frangioni1,3 "Image-Guided Surgery using Invisible Near-Infrared Light: Fundamentals of Clinical Translation"Mol Imaging. 2010 October ; 9(5): 237–255.

39) Feifan Zhou, Da Xing, ZhongminOu, Baoyan Wu, Daniel E. Resasco and Wei R. Chen "Cancer photothermal therapy in the near-infrared region by using single-walled carbon nanotubes" Journal of Biomedical Optics 14 2, 021009 March/April 2009.

40) Wei R. Chen, Robert L. Adams , Aaron K. Higgins, Kenneth E. Bartels, Robert E. Nordquist. "Photothermal effects on murine mammary tumors using indocyanine green and an 808-nm diode laser: an in-vivo efficacy study" Cancer Letters 98 (1996) 169-173

41) Sunil Krishnan, Parmeswaran Diagaradjane, and Sang Cho. "Nanoparticle-mediated thermal therapy: Evolving strategies for prostate cancer therapy" Int J Hyperthermia. 2010; 26(8): 775–789.

42) V. G. Liu, T.M. Cowan, S.-W. Jeong, S.L. Jacques, E.C. Lemley and W.R. Chen. “Selective Photothermal Interaction Using an 805-nm Diode Laser and Indocyanine Green in Gel Phantom and Chicken Breast Tissue” Lasers Med Sci 2002, 17:272–27

43) Christos Haritoglou, Wolfgang Freyer, Siegfried G. Priglinger and Anselm Kampik “Light absorbing properties of indocyanine green (ICG) in solution and after adsorption to the retinal surface — an ex vivo approach” Graefe's archive for clinical and experimental ophthalmology, Volume 244, Number 9, 1196-1202

44) J D Byrne, T Betancourt, L Brannon-Peppas. “Active targeting schemes for nanoparticle systems in cancer therapeutics” Adv Drug Deliv Rev. 2008 Dec 14; 60(15):1615-26.

45) Zhou J, Liu W, Pong RC, Hao G, Sun X, Hsieh JT.” Analysis of oligo-arginine cell-permeable peptides uptake by prostate cells.” Amino Acids. 2010 Dec

46) Omid C. Farokhzad, Sangyong Jon, Ali Khademhosseini, Thanh-Nga T. Tran, David A. LaVan, and Robert Langer. “Nanoparticle-Aptamer Bioconjugates: A New Approach for Targeting Prostate Cancer Cells” CANCER RESEARCH 64, 7668–7672, November 1, 2004.

47) Shanta Dhara, Frank X. Gu, Robert Langer, Omid C. Farokhzad, and Stephen J. Lippard. “Targeted delivery of cisplatin to prostate cancer cells by aptamer functionalized Pt (IV) prodrug-PLGA–PEG nanoparticles” Proc Natl Acad Sci U S A. 2008 Nov 11;105(45).

48) http://www.coherent.com/

49) http://us.flukecal.com/

50) http://www.omega.com/techref/themointro.html

51) Mohammad A. Yaseen, Jie Yu, Michael S. Wong, and Bahman Anvari. “Laser-Induced Heating of Dextran-Coated Mesocapsules Containing Indocyanine Green” Biotechnol. Prog. 2007, 23, 1431-1440

52) http://www.ecomm.baxter.com

53) Richard M. Levenson, David T. Lynch, Hisataka Kobayashi, Joseph M. Backer, Marina V. Backer.” Multiplexing with Multispectral Imaging: From Mice to Microscopy”. ILAR J. 2008;49(1):78-88

54) http://www.cri-inc.com/products

55) Daniel L. Farkas, Congwu Du, Gregory W. Fisher, Christopher Lau, Wenhua Niu, Elliot S. Wachman, Richard M. Levenson. “Non-invasive image acquisition and advanced processing in optical bioimaging”. Computerized Medical Imaging and Graphics 22 (1998) 89–102

BIOGRAPHICAL INFORMATION

Ronak Patel was born in Devgad Baria, India in February 1986. She pursued her Bachelor in Biomedical Engineering from Government Engineering College at Gandhinagar, Gujarat University, India, and graduated in June 2009. To acquire more knowledge and experience, she joined the Master of Science in biomedical engineering program at the University of Texas at Arlington in January 2010. She found Medical Imaging interesting and emerging field of research. She joined Biomedical Optics Laboratory in May 2010. She started working on polymeric Nano particulate system for cancer diagnosis and therapy using various optical imaging modalities. She intends to continue working in a research environment in the field Optical Imaging involving fluorescence imaging and NIR spectroscopy.